Publisher: GSA
Journal: GSAB: GSA Bulletin
DOI:10.1130/B31266.1

Space-time evolution of the Neogene–Quaternary Kuh-e-Faghan fault, central Iran
GSA Bulletin; Month/Month 2015; v. 1xx; no. X/X; p. 000–000; doi: 10.1130/B31266.1

Spatio-temporal evolution of intraplate strike-slip faulting: the Neogene-Quaternary Kuh-e-Faghan Fault, Central Iran

Gabriele Calzolari[(1)], Federico Rossetti[(1;*)], Marta Della Seta[(2)], Reza Nozaem [(3)], Valerio Olivetti[(4)], Maria Laura Balestrieri[(5)], Domenico Cosentino[(1)], Claudio Faccenna[(1)], Finlay M. Stuart[(6)], Gianluca Vignaroli[(1)]

[1]*Dipartimento di Scienze, Università Roma Tre, Largo S. L. Murialdo 1, 00146 Roma, Italy*
[2]*Dipartimento di Scienze della Terra, "Sapienza" Università di Roma, Piazzale Aldo Moro 5, 00185 Rome, Italy*
[3]*Department of Geology, Imam Khomeini International University, 34149-16818 Qazvin, Iran*
[4]*Aix-Marseille Université, CNRS, IRD, CEREGE UM34, 13545 Aix en Provence, France.*
[5]*CNR-Istituto di Geoscienze e Georisorse, Via G. La Pira 4, 50121 Firenze, Italy*
[6]*Scottish Universities Environmental Research Centre, Scottish Enterprise Technology Park, East Kilbride G75 0QF, UK*

(*) Corresponding Author
Email: federico.rossetti@uniroma3.it
Tel: +390657338082
Fax: +3957338201

ABSTRACT

Central Iran provides an ideal region to study the long-term morphotectonic response to the nucleation and propagation of intraplate faulting. In this study, a multidisciplinary approach that integrates structural and stratigraphic field investigations with apatite (U+Th)/He (AHe) thermochronometry is used to reconstruct the spatio-temporal evolution of the Kuh-e-Faghan Fault (KFF) in northeastern Central Iran. The KFF is a narrow, ca. 80 km long, deformation zone that consists of three main broadly left stepping, E-W trending, dextral fault strands that cut through the Mesozoic-Paleozoic substratum and the Neogene-Quaternary sedimentary cover. The AHe thermochronometry results indicate that the intra-fault blocks along the KFF experienced two major episodes of fault-related exhumation at ~18 Ma and ~4 Ma. The ~18 Ma faulting/exhumation episode is chiefly recorded by the structure and depositional architecture of the Neogene deposits along the KFF. A source-to-sink scenario can be reconstructed for this time frame, where topographic growth caused the synchronous erosion/exhumation of the pre-Neogene units and deposition of the eroded material in the surrounding fault-bounded continental depocenters. Successively, the KFF gradually entered a period of relative tectonic quiescence and, probably, of regional subsidence during which a thick pile of fine-grained onlapping sediments were deposited. This may have caused resetting of the He ages of apatite in the pre-Neogene and the basal Neogene successions. The ~4 Ma faulting episode caused the final exhumation of the fault system, resulting in the current fault zone and topography. The two fault-related exhumation episodes fit with the regional early Miocene collision-enhanced uplift/exhumation, and the late Miocene–early Pliocene widespread tectonic reorganization of the Iranian plateau. The reconstructed long-term, spatially and temporally punctuated fault system evolution in intraplate Central Iran during Neogene-Quaternary times may reflect states of far-field stress changes at the collisional boundaries.

INTRODUCTION

As demonstrated by regional and global stress field maps, in-plane stresses can be transferred from the plate margins across large distances, through continental and oceanic lithosphere (e.g. Zoback, 1992; Sandiford et al., 2004 Cloetingh et al., 2005; Heidbach et al., 2008). This is best illustrated in regions affected by continental collision, where seismicity extends deep into the continental plate interiors, thus defining broad and diffuse zones of deformation (e.g. Central Iran, Turkey and Tibetan plateau; Hatzfeld and Molnar, 2010). In such settings, the transmission of compressive stresses and distribution of deformation in intraplate settings are dominantly a function of the spatial and temporal changes in plate boundary dynamics (Raimondo et al., 2014) and, in particular, of the degree of tectonic coupling at the collisional interface (Ellis, 1996; Ziegler et al., 1998).

Studies on intraplate deformation demonstrate that strike-slip faulting is the primary process by which such horizontal movements are accommodated and stresses are transferred further away from the collision front (e.g. Molnar and Tapponnier, 1975; Bayasgalan et al. 1999; Calais et al., 2003; Storti et al. 2003; Vernant et al., 2004; Simons et al., 2007; Reece et al., 2013; Allen et al., 2011; Walpersdorf et al., 2014). Strike-slip dominated continental deformation zones typically consist of interlinked systems of fault- and shear zone-bounded blocks that partition strain to form complex regions of displacement, internal distortion and rigid block rotations at various scales (e.g. Ron et al., 1984; Christie-Blick and Biddle 1985; Sylvester, 1988; Woodcock and Schubert 1994; Storti et al., 2003; Cunningham and Mann, 2007). This is mostly due to the structural inheritance of continental crust and lithosphere, acquired through the continuous incorporation of plate margin structures by continental collision and accretion processes that operate for geologically long periods (e.g., Molnar, 1988; Ziegler et al., 1998; Matenco et al., 2007; Dyksterhuis and Müller, 2008; Aitken et al., 2013; Raimondo et al., 2014). Such structures constitute major sub-vertical weak zones of

89 mechanical anisotropy and strain softening, which, once incorporated into the plate interiors,
90 may be readily reactivated as strike-slip dominated deformation zones at various spatial and
91 temporal scale (e.g., Tapponier and Molnar, 1977; Sutton and Watson, 1986; Salvini et al.,
92 1997; Tavarnelli, 1998; Tavarnelli and Holdsworth, 1999; Tavarnelli and Pasqui, 2000;
93 Holdsworth et al., 2001; Webb and Johson, 2006; Allen et al., 2011; Rossetti et al., 2003;
94 Morley, 2007; Di Vincenzo et al., 2013; Avouac et al., 2014). The longevity of intraplate
95 strike-slip fault systems and their linkage to plate boundary dynamics makes them excellent
96 strain markers of the intraplate deformation response to continental collision. An
97 understanding of the spatial and temporal distribution of crustal deformation accommodated
98 along strike-slip faults is therefore central to unravel regimes and modes through which
99 continental tectonics operate.

100 The cause of crustal strain, topographic growth and exhumation along strike-slip
101 faults is a complex feedback between near-field (<20 km) boundary conditions and far-field
102 plate tectonic driving mechanisms (Spotila et al., 2001; Buscher and Spotila, 2007).
103 Moreover, several processes and conditions have been invoked to explain topographic growth
104 and focused exhumation along strike-slip systems and these processes may play an important
105 role in regional exhumation and topographic patterns: (1) the degree of obliquity of the plate
106 motion vector with respect to the fault trace (e.g. Sanderson and Marchini, 1984; Fitzgerald et
107 al., 1993; 1995; Spotila et al., 1998); (2) structural irregularities such as stepovers (Aydin and
108 Nur, 1985; Hilley and Arrowsmith, 2008; Finzi et al., 2009; Carne and Little, 2012), (3)
109 variations in master fault dip (Dair and Cooke, 2009); (4) enhanced erosion due to pervasive
110 tectonically induced fracturing and associated volume increase (Braun, 1994; Schopfer and
111 Steyrer, 2001; Le Guerroué and Cobbold, 2006; Molnar et al., 2007; Schrank and Cruden,
112 2010; Cox et al., 2012),); and (5) climate forcings (Headley eta l., 2013; Pavlis et al., 2014).
113 Furthermore, the amount of exhumation along a strike-slip fault is not always simply

114 correlated with the degree of transpression or with the composition of the juxtaposed rocks
115 (Spotila et al., 2007).
116 This study describes the Neogene-Quaternary structural and stratigraphic evolution
117 and exhumation history of the Kuh-e-Faghan Fault (KFF) system, a major shear belt situated
118 at the northern margin of the Lut Block in Central Iran (Fig. 1). The aim is to understand: (i)
119 how intraplate tectonic deformation propagates and evolves in space and time; and (ii) its
120 impact on the long-term, fault-controlled landscape evolution. Field studies are integrated
121 with apatite (U+Th)/He (AHe) thermochronometry to link structures to the distribution of
122 topographic relief and spatial variations in exhumation rate. We document E-W oriented
123 dextral strike-slip tectonics associated with two distinct episodes of fault-related exhumation
124 at ~18 Ma and ~4 Ma. A conceptual model of fault initiation and propagation is then
125 proposed that has implications for the activation and kinematic evolution of the intraplate
126 strike-slip fault systems in Central Iran during Neogene-Quaternary times.
127
128 **GEOLOGICAL BACKGROUND**
129 The Arabia-Eurasia collision zone is one of the largest and most spectacular examples
130 of continental convergent deformation on Earth (Hatzfeld and Molnar, 2010). Convergence
131 may have initiated in the mid-Jurassic (e.g. Agard et al., 2011) and culminated with the
132 Arabia–Eurasia continental collision through a polyphase tectonic history that involved the
133 following phases: (i) Collision is estimated to have started at the Eocene–Oligocene boundary
134 (e.g. Hessami et al., 2001; McQuarrie et al., 2003; Hafkenscheid et al., 2006; Robertson et al.,
135 2006; Vincent et al., 2007; Allen and Armstrong, 2008; Homke et al., 2009; 2010;
136 Mouthereau et al., 2012). (ii) A regional increase in collision-related uplift, exhumation, and
137 subsidence in adjacent basins, began in the early Miocene, as documented by low-
138 temperature thermochronometric (Axen et al., 2001; Guest et al., 2006; Verdel et al., 2007;

139 Gavillot et al., 2010; Homke et al., 2010; Okay et al., 2010; Khadivi et al., 2012; Ballato et
140 al., 2013; Madanipour et al., 2013;), stratigraphic (e.g. Hessami et al., 2001; Guest et al.,
141 2006; Mouthereau et al., 2007; Ballato et al., 2008; Morley et al., 2009; Khadivi et al., 2010;
142 Ballato et al., 2011) and structural (e.g. Allen et al., 2004; Mouthereau et al., 2007) evidence.
143 (iii) A widespread tectonic reorganization during late Miocene–early Pliocene is attested by
144 enhanced exhumation in the Alborz and Talesh mountains (Axen et al., 2001; Rezaeian et al.,
145 2012; Madanipour et al., 2013), fault kinematic changes in the Kopeh Dagh (Shabanian et al.,
146 2009a; Shabanian et al., 2009b; 2010; Robert et al., 2014) and in the Zagros–Makran transfer
147 zone (Regard et al., 2005), which are thought to have resulted in the current regional
148 kinematic configuration (Allen et al., 2004). The evidence gathered in those studies
149 principally comes from the orogenic belts situated at the edges of the Iranian plateau (Fig. 1;
150 Zagros Alborz, Kopeh Dagh and Talesh). In contrast, little is known about the deformation
151 history of the intraplate domain of Central Iran.
152 The Central East Iran Microcontinent (CEIM) consists of an amalgamation of
153 continental blocks bordered by topographically prominent mountain ranges, comprising the
154 Kopeh Dagh, Alborz and Talesh orogenic belts to the north, and the Zagros orogenic belt and
155 Makran active subduction related complex to the north-west and south (Fig. 1). In particular,
156 the CEIM includes the Lut, Tabas, and Yazd microblocks (Aghanabati, 2004), which are
157 bounded by linear mountain-belts developed along major strike-slip fault zones that each
158 have their distinct stratigraphy, deformation style and pattern of recent seismicity (Berberian
159 and King, 1981; Berberian, 2014).
160 The GPS displacement vectors indicate a NNE motion of the Arabian plate relative to
161 Eurasia of ~25 mm/yr (Sella et al., 2002; McClusky et al., 2003; Vernant et al., 2004;
162 Reilinger et al., 2006; Walpersdorf et al., 2014). Such convergence is mostly absorbed in the
163 orogenic terrains through contractional deformation (Zagros, Alborz, Kopeh Dagh and Talesh

164 in the north) (Fig. 1). The CEIM is moving northward at 6–13 mm/yr with respect to the
165 stable Afghan crust at the eastern edge of the collision zone (Walpersdorf et al., 2014). Such
166 differential motion is largely accommodated by the active strike-slip faults systems bounding
167 the CEIM, which are organized into N-S dextral (from west to east: the Deshir, Anar,
168 Nayband–Gowk, and Nehbandan faults) and E–W sinistral (from north to south: Doruneh and
169 Dasht-e Bayaz faults) shears (Fig. 1). Various studies detailed present kinematics and total
170 cumulative shear along the active strike-slip faults systems of Central Iran, using geologic
171 and geomorphic displaced markers identified from satellite imagery (Walker and Jackson,
172 2004; Allen et al., 2004; 2011; Meyer et al., 2006; Meyer and Le Dors, 2007; Farbod et al.,
173 2011). Taking into account the present-day slip rates (~2-10 mm/yr) along the major fault
174 systems, the onset of strike-slip tectonics is inferred to date back to ~5 Ma (Allen et al.,
175 2004). This shear pattern is commonly assumed to be accompanied by diffuse rigid block
176 rotation and strain partitioning during ongoing Arabia-Eurasia convergence (Jackson and
177 McKenzie, 1984; Walker et al., 2004; Walker and Jackson, 2004; Walker and Khatib, 2006;
178 Fattahi et al., 2007; Allen et al., 2011; Farbod et al., 2011). Significant, post-Miocene
179 counter-clockwise rotation (25-35°), assumed to be accommodated along the major N-S
180 striking dextral fault systems, was documented in the Lut and Tabas blocks, whereas no
181 significant rotation has been detected north of the Doruneh Fault (Mattei et al., 2012). In
182 particular, modeling the GPS data with a block rotation model suggests that the rotations
183 have been going on at a similar rate (1 ± 0.4°/Ma) over the last 12 Ma (Walpersdorf et al.,
184 2014). Nonetheless, evidence is provided to indicate that Deshir and Anar faults (Fig. 1) are
185 accommodating relative motion between non rotating blocks and strike-slip faulting is not
186 confined to the Lut edges but also occurs in Central Iran, suggesting a non-rigid behaviour of
187 the CEIM at least during the last 25 Ma (Meyer et al., 2006; Meyer and LeDortz, 2007).

In a recent study, Nozaem et al. (2013) documented important post-Neogene to Quaternary dextral strike-slip tectonics along the Kuh-e–Sarhangi Fault on the north-western edge of the Lut block (Fig. 1), less than 40 km south of the sub-parallel, active sinistral Doruneh Fault (Tchalenko et al., 1973; Fattahi et al., 2007; Farbod et al., 2011). This post-Neogene faulting is proposed to have occurred due to the tectonic reactivation of the northeastward extension of the late Neoproterozoic to early Paleozoic Kashmar–Kerman Tectonic Zone (Ramezani and Tucker, 2003; Rossetti et al., 2015; Fig. 1) in response to a kinematically induced stress field scenario (Nozaem et al., 2013). Similarly, Javadi et al. (2013) documented a polyphase kinematic history for the Doruneh Fault, with a change from dextral to sinistral motion during the late Miocene-early Pliocene times.

THE KUH-E-FAGHAN FAULT ZONE

Our study focuses on a linear mountainous ridge (~80 km long and ~15 km wide; maximum elevation of ~1700 m), associated with the E-W oriented Kuh-e-Faghan Fault (KFF, Figs. 1-3). This fault system forms the northern termination of the Kuh-e–Sarhangi fault system (Nozaem et al., 2013) and is located 25 km south of the Doruneh Fault, continuing eastward for ~80 km (Fig. 2). The KFF system and the surrounding areas are seismically active (Fig. 2) , with maximum recorded seismic magnitude between 4 and 5.5 and focal depths <35 km (Farbod et al., 2011).

The KFF is an E-W oriented brittle deformation zone that cuts pre-Neogene units (Paleozoic-Mesozoic successions, made of slightly or unmetamorphosed carbonates, subordinate shales and sandstones; hereafter referred as basement units) and the unconformably overlying Neogene and Quaternary continental successions (Eftekhar-Nezhad et al., 1976; Behroozi et al., 1987; Jalilian et al., 1992; Ghomashi et al., 2001) (Fig. 3). Fault kinematics along the KFF is poorly described, with strike-slip (Eftekhar-Nezhad et al., 1976;

213 Behroozi et al., 1987; Jalilian et al., 1992; Ghomashi et al., 2001) or reverse (Hassami et al.,
214 2003; Javadi et al., 2013) kinematics having been proposed.

215 Paleogeographic and sedimentological studies (Berberian and King, 1981; Amini,
216 1997) refer the Neogene deposits alongside the KFF to the Upper Red Formation of Central
217 Iran (Berberian, 1974). The Upper Red Formation is the oldest continental deposit
218 unconformably lying above the marine, late Oligocene–middle Miocene Qom Formation
219 (Berberian, 1974; Deneshian and Ramezani Dana, 2007; Ballato et al., 2008; Hadavi et al.,
220 2010). It consists of km-thick alternating conglomerates, sandstones, siltstones, marls and
221 evaporites (Amini, 1997; Ballato et al., 2008; Morley et al., 2009; Ballato et al., 2011). Due
222 to the lack of biostratigraphical markers or radiometric lly datable units, the age and duration
223 of the Upper Red Formation are not well constrained. Based on the magnetostratigraphic
224 study of the Eyvanekey section in southern Alborz Mountains, Ballato et al. (2008) proposed
225 a Burdigalian to Tortonian (17.5-7.5 Ma) age.

226 Quaternary successions unconformably cover the Upper Red Formation deposits and
227 consist of alluvial fans and terraced alluvial plain deposits. Similar generations of alluvial
228 fans, as well as regional arrangement of river terraces have been recognized in the
229 neighbouring regions of eastern Iran and explained in terms of Late Pleistocene and Holocene
230 environmental changes (Walker and Fattah, 2011). In particular, an infrared optically
231 stimulated luminescence age of ≤10 ka (end of the Last Glacial Maximum) was obtained for
232 the deposition of the Shesh–Taraz fan along the Doruneh fault (Fig. 1; Fattahi et al., 2007).
233

234 **NEOGENE STRATIGRAPHY**

235 The Upper Red Formation of the study area is a ~4 km thick fining-upward succession
236 of continental deposits, which include three main unconformity-bounded stratigraphic units,
237 hereafter referred as sedimentary Cycle-1, Cycle-2, and Cycle-3, respectively (Figs. 3-5). The

general stratigraphy is shown in Figure 4A and the schematic generalised vertical sections, together with the corresponding stick-logs for the northern and southern area of the KFF are reported in Figure 5. The estimated thickness variations have been measured along seriate transects shown in Fig. 3.

Cycle-1

Cycle- 1 consists of breccias (Ng-B) that distally evolve into crudely stratified conglomerates (hereafter referred to as Ng-C), which lie above a major angular unconformity (Fig. 4B) onto pre-Neogene rocks. Cycle-1 shows large lateral thicknesses variations. In particular, the basal talus Ng-B breccias occur only along the western part of the study area (Fig. 3). Their thickness varies strongly across-strike of the KFF from south to north, reaching up to ~450 m and ~100 m, respectively (Fig. 5). The overlying alluvial fan conglomerates of Ng-C are thickest (~500 m) along the geological cross-section A-B (Fig. 3), but, more commonly, does not exceed 300 m in thickness (Fig. 5).

The majority of the conglomerates and breccias are clast-supported, but transition into matrix supported conglomerates occurs in places in the upper part of the cycle. The matrix (up to 25%) is usually made of dark red to pale grey mudstone and siltstone. Clasts making up the bulk of the basal deposits have been directly sourced from the proximal pre-Neogene substratum. The clasts vary from boulder to cobble size. Here we interpret these breccias (Ng-B) as talus deposits sourced by the local linear mountain ridge whereas the Ng-C conglomerates are interpreted as to alluvial fan deposits. In places, the basal deposits include boulder (up to 1-3 m^3 in volume) deposits made of breccias and/or conglomerates, indicating reworking of the older part of Cycle-1 deposits. Transition to the upper part of Cycle-1 varies from gradual to sharply on an angular unconformity (Fig. 4B). Where basal breccias are absent the upper part of Cycle-1 unconformably overlies the basement units with deposits

consisting of clast-supported, crudely- to well-stratified polymictic conglomerates, with relatively rounded and sorted clasts. In places, imbricated clasts, arranged in 0.5 to 3.5 m-thick lenticular and, at times, laterally discontinuous beds point to fluvial channel deposits.

According to differences in lithofacies from the upper part of the Cycle-1, a distinction can be made between the western and eastern areas. Along the western area, the conglomerates generally exhibit less rounded and more chaotically organized clasts, with matrix-rich horizons showing convolute sedimentary structures. In contrast, along the eastern sector, the conglomerate deposits are typically interbedded with subordinate, fining upwards, 10 to 50 cm thick sandstones packages. Concave upwards erosional surfaces and lenticular beds geometries are common. These differences in the Cycle-1 lithofacies could be related to the presence of more unstable sedimentary basin linked to uplifting local source areas in the western part with respect to the eastern region of the study area.

Cycle 1 is interpreted as a high-energy deposit. The poorly-sorted, texturally immature and chaotic nature of the basal breccias, coupled with the clast lithology all suggest very proximal deposition on steep slopes by block fall and in proximal fans and/or as talus cones. The laterally continuous nature of the upper part of Cycle-1 deposits also suggests that deposition occurred within an alluvial fan complex in the west area and a broad, well-fed alluvial plain to the east.

Cycle-2

Cycle-2 consists of decimetre-thick bedded, well-sorted, mineralogically and texturally immature medium to coarse silty red sandstone (hereafter referred to as Ng-SSi). Cycle-2 is absent in the westernmost part of the KFF and generally increase in thickness eastward, where it reaches its maximum (~580 m) along geological transects G-H and I-J

(Figs. 3 and 5). Progressive angular unconformities affecting those continental deposits are very common, especially in the lower part of Cycle-2 (Fig. 4C).

Cycle-2 Ng-SSi usually shows planar- to cross-lamination, and unconformably cover the Ng-C deposits. In places, the Ng-SSi deposits are characterized by trough cross-bedding alternating with subordinate horizons of coarse gravelly sandstones. Straight-crested symmetric, lunate and linguoid ripples are all common feature of the Cycle-2 deposits, together with locally bioturbated horizons and surfaces exhibiting mud cracks and casts (Fig. 4C), which represent the channel/bank and overbank deposits, respectively.

We interpret Cycle-2 deposits as related to a fluvio/palustrine environment possibly proximal to a wide, well-fed alluvial plain capable of being supplied by relatively well-sorted material. The close proximity of the source produced mineralogically and texturally mature sediments.

Cycle-3

Cycle-3 **de**posits form two distinct units, Ng-GM and Ng-MS (Figs. 3, 4D, 5). The basal unit Ng-GM shows a distinct angular unconformity at the base (Fig. 4D), and consists of a marly succession and subordinate gypsum horizons. It is absent in the western part of the KFF, and reaches its maximum thickness (~450 m; Figs. 3 and 5) in the central sector of the study area and then thins out eastward. Some fine sandstone beds, tens of centimetre-thick, are also present, with infrequent planar- to cross-laminated horizons. Desiccation cracks and mud casts are also common (Fig. 4D). The gypsum horizons, up to a few 10s cm thick ,are typically secondary, showing a displacive character of the gypsum crystals, which also occur along bedding surfaces and fractures. In places, this secondary origin for the gypsum layers is responsible for the deformation and disruption of the original layering. The basal and upper part of the Ng-GM unit are characterized by meter-thick red marls and silts, relatively free of

312 gypsum, interbedded with pale yellow gypsiferous silty marls, while the central portion is
313 characterised by continuous thick packages of pale yellow gypsiferous silty marls.
314 The subsequent Ng-MS unit conformably overlies Ng-GM deposits. It consists of a
315 few 10s cm of pale red to beige, massively-bedded marls and silty-mudstones, with
316 millimetre scale layering. These are interbedded with subordinate 0.5 to 2.5 m-thick cross-
317 bedded, at times laterally discontinuous, light brown, medium to coarse sandstones. Bedding
318 surfaces exhibiting small-scale straight crested asymmetric ripples are rare uncommon but
319 not rare. The Ng MS unit extends throughout the northern KFF area, reaching a maximum
320 thickness of ~1230 m (transect IJ in Fig. 3; Fig. 5)
321 The Ng-GM unit is inferred to have been deposited under different climate conditions,
322 ranging from dry episodes, characterized by evaporation dominated events (secondary
323 gypsum grew within sediments), to wetter condition, indicated by suspension-dominated
324 deposits (massive and layered marls and silty-mudstones) or deposits formed in an
325 environment with a relatively high energy tractional and unidirectional turbulent flow
326 (rippled silty-marls and fine sands). Such sedimentary characteristics are representative of
327 playa mud flats and playa lake environments (Reading, 2009). The marls and silty-mudstones
328 of the Ng-MS unit, mainly characterized by millimetre-scale layering and some rare rippled
329 surfaces, are indicative of deposition in wet period from a low energy shallow lacustrine
330 environment, where deposition occurred primarily by suspension settling and secondarily by
331 laminar and turbulent flow. The subordinate meters-thick cross-bedded sandstone were
332 deposited by more turbulent and energetic flow and represent deposition during periods of
333 increased sediment supply from riverine input.
334
335 **STRUCTURE**

336 The basement units exhibit a steeply-dipping ENE-WSW oriented planar fabrics,
337 similar to the neighbouring Kuh-e-Sarhangi Fault system (Nozaem et al., 2013). The
338 Neogene deposits show bedding attitudes dipping away from, and striking sub-parallel to the
339 axis of the topographic divide, arranged to form a broad eastward plunging anticline.
340 Moreover, the bedding dip angle of the Neogene deposits generally decreases away from the
341 boundary fault system (see the geological map in Fig. 3).
342 The KFF system consists of three, broadly left-stepping, E-W striking fault strands,
343 hereafter referred as the western (WFS) and central (CFS) fault strands that abut the NW-SE
344 to E-W striking eastern fault strand (EFS) (Fig 3). The fault strands have along-strike lengths
345 of 30 to 40 km and their associated fault damage zones bound E-W elongated ridges. We
346 measured 501 striated fault surfaces (over a total number of 1040 structural data) occurring in
347 the basement units, the Neogene and Quaternary deposits were measured in the field. Fault
348 kinematics was obtained based on classical criteria for brittle shear zones, such as fault offset,
349 growth fibres, and Riedel shears (Petit, 1987; Doblas, 1998). Fault orientation analysis was
350 performed using the software Daisy 3 (Salvini, 2004; http://host.uniroma3.it/progetti/fralab).
351 The faults show high-to sub-vertical dips, with a maximum frequency distribution at 85° and
352 a mean dip value of 75°. The fault strikes show a maximum at N94°, with subordinate N131°
353 and N47°. The frequency distribution of the pitch angle (counted positive in the plane from
354 the fault strike) of the measured slickenlines shows dominant strike-slip kinematics with
355 maxima at 12° and 162° and subordinate dip-slip population (84°). In particular, the analysis
356 shows that ~72% of the slickenline pitches are in the range 0°-45° and 135°-180° and less
357 than 28% exhibit 45° to 135° pitches. The mean pitch values is 2° (see inset in Fig. 3).
358 In the following sections, a systematic description of the fault system geometry and
359 kinematics along the main fault strands is provided.
360

361 **Western fault strand**

362 The WFS runs W-E for more than 35 km on the southern side of the KFF, with
363 variations along-strike (Fig 3). The western fault tip is defined by a broad (wavelength of ~5
364 km), E-W striking, south-verging monocline that affects the basal Ng-C deposits. The fold
365 axial trace maps out ~ 20 km and separates gently north-dipping (< 20°) strata to the north
366 from steeply south-dipping (>40°) strata to the south, narrowing to the east (Fig. 3). The fault
367 planes rarely cuts through Ng-C strata and therefore the fault is considered as mostly blind
368 (Fig. 3). Moving eastward along the WFS trace, the southern limb of the monocline becomes
369 increasingly steeper to overturned and is dissected by numerous subvertical fault strands (see
370 the geological cross-section A-B in Fig. 3 and Fig. 6A). These fault strands define a ~50 m
371 wide fault damage zone, made of vertical, E-W striking fractured rock panels along which
372 abrupt contacts between the basal Neogene conglomerates (Ng-C) and the gypsiferous marls
373 (Ng-GM) occur (Fig. 6A). Shearing is dominantly localised along E-W striking dextral slip
374 zones, associated with smaller synthetic NW-SE striking faults (stereoplot in Fig. 6A).

375 Further to the east, the WFS bends NE to form a major restraining bend that affects
376 the Neogene deposits, with positive flower structures in cross-section and a contractional
377 strike-slip duplex (Woodcock and Fischer, 1986) in map view (see geological map and cross-
378 sections E-F and E2-F2 in Fig. 3). The duplex-bounding faults are developed within the
379 Neogene deposits; however, faults also affect the Quaternary alluvial deposits (see below).
380 The restraining bend is associated with development of a tight NE-SW trending syncline,
381 mapping out subparallel to the main fault trace and affecting the Ng-C and the unconformable
382 Ng-SSi deposits. The fold profile shows a moderately north-dipping southeastern flank with a
383 steep to overturned northwestern flank, with a periclinal doubly plunging geometry (Fig. 3).
384 The north-western fold limb is dissected by NE striking sub-vertical fault strands that cause
385 the tectonic repetitions among the Neogene units. The duplex-bounding faults are subvertical,

386 with fault slip localization occurring along the northwestern boundary fault zone. This fault
387 zone consists of a ~300 m wide damage zone, defined by subvertical panels of cataclastic
388 fault rocks and cohesive fault breccias (Fig. 6B). Dextral kinematics is attested by drag
389 folding of the Neogene strata along the principal displacement zone (Figs. 6C). Measured
390 fault surfaces strike NE-SW; offset bedding truncations, Riedel shears and calcite
391 slickenfibers, systematically document either dextral oblique strike-slip or reverse kinematics
392 (stereoplot in Fig. 6C).
393
394 **Central fault strand**
395 The CFS runs W-E for about 30 km on the northern side of the KFF, defining a sharp
396 break in slope between the topographically elevated pre-Neogene substratum and the
397 Neogene-Quaternary sedimentary covers (Fig. 3). Basement-cover relations are well
398 preserved in the central part of the CFS, with fault zone localization occurring within the
399 basement units and only marginally within the Neogene deposits (Ng-C and Ng-GM) units
400 (cross-sections A-B and C-D in Fig. 3). In the field, they generally appear as broad (up to 100
401 m wide) deformation zones, associated with vertical rock panels affected by diffuse brittle
402 deformation. The shear deformation is principally accommodated within the weaker
403 basement shale beds, while the stronger sandstones remain partially coherent to define fault
404 lithons (Fig. 7A). The slip zones are typically delocalized, defined by bands of cataclastic
405 material, meters to tens of meters thick. As in the WFS, well-developed fault surfaces with
406 striations and kinematic indicators occur, but localized slip zones and fault gouges are rarely
407 exposed. Brittle deformation in the Ng-C deposits is characterized by a dominant set of sub-
408 vertical E-W striking cataclastic zones, generally less than 1 m thick. Striated fault surfaces
409 provide sub-horizontal pitch values and the fault kinematics is systematically dextral.

Subsidiary, steeply-dipping NW-SE dextral and NNE-SSW sinistral faults are also reported (see the stereoplot in Fig. 7A).

Continuing to the east, the CFS bends southward and branches out into four main NW-SE oriented subvertical fault segments, that in map view are arranged to form a 10 km wide, trailing extensional imbricate fan (Woodcock and Fischer, 1986), also referred as to "horsetail-type" transtensive termination (Granier, 1985) (Fig. 3). The dominant strike-slip motion along the CFS passes into a lozenge-shaped zone of extension or transtension at its tip, consistent with dextral offset, which is filled up by the Ng-GM deposits (Fig. 3). Striated fault surfaces either show dip-slip normal or oblique-to-strike-slip dextral kinematics. Faulting within the Ng-GM deposits is accommodated by diffuse zones of deformation, hundreds of meters wide, characterized by evenly spaced (meters apart) sets of NW-SE striking faults that accommodate both oblique-slip and normal dip-slip displacements. Many of these mesoscale faults show offsets that die out upward and some of them die out vertically, indicating syn-depositional faulting (Fig. 7B).

Eastern fault strand

The EFS is a ~ 40 km long, sub-vertical fault zone, made of the coalescence of several synthetic faults to form a curvilinear slip zone and prominent range front, striking from NW-SE to E-W at its eastward termination (Fig. 3). The fault zone shows a decametre-to-hectometre thick damage zone that comprises numerous mesoscale fault segments cutting through the pre-Neogene basement units that are tectonically juxtaposed against the Ng-GM successions. In particular, the NW segment abruptly cuts an E-W striking Neogene basin boundary fault strand. It continues eastward bending to E-W direction, showing a prominent linear fault scarp in the Neogene deposits that can be traced continuously eastward for more than 20 km in the Quaternary alluvial plain (Fig. 8A). Where the fault zone bends to an E-W

435 direction the fault damage zone widens to more than 200 m wide and has prominent fault
436 cores, up-to-tens of meter thick. The fault cores consist of ultracataclastic bands and fault
437 gouges, separated by brecciated fault rocks and sheared lithons (Fig.8B). Major fault surfaces
438 are typically sub-vertical, NW-SE and E-W striking and exhibit sub-horizontals slickenlines
439 (pitch: 5-15°). Most of the striated fault surfaces have hematite coatings. Fault kinematics as
440 deduced by synthetic Riedel shear planes, together with calcite slickenfibers, grain grooves
441 and lunate fractures systematically point to dominant dextral slip (Figs. 8C-D). Decameter-
442 scale S-C fabrics are observed along coherent tracts of the principal displacement zone of the
443 EFS and continue over significant distances (> 300 m), both along the basement-Neogene
444 contacts and within the Neogene deposits (Figs. 9A-B). Within these deformation zones, S
445 surfaces are defined by dissolution seams and strike NW-SE, the C-surfaces strike roughly E-
446 W to ENE-WSW. Lineations are provided by slickenlines on the C-surfaces that
447 systematically are subhorizontal. The S-C fabrics are associated with NW-SE striking,
448 steeply dipping joint and calcite- and gypsum-bearing vein sets, indicating dextral shearing
449 (Fig. 9C). Meter-thick cohesive and foliated cataclasites are observed in places to form the
450 fault rocks along the slip zones developed within the Neogene deposits.
451
452 **Quaternary faulting**
453 The Quaternary successions along the KFF consist of a wide variety of alluvial fan
454 and fluvial deposits, made of conglomerates, gravels and sands exhibiting various degree of
455 consolidation. These deposits lie upon a regional erosional surface (pediment) cut through the
456 strongly tilted Neogene units (Figs. 6B and 8A). Quaternary faults and joints occur along the
457 WFS and the EFS (see Fig. 3 for site locations), where faulting is dominated by dextral fault
458 zones.

459 Along the contractional bending at the eastern end of the WFS, dextral and oblique-
460 slip faults cut through the Quaternary terraced deposits, juxtaposing and squeezing together
461 lenses of Quaternary and Neogene sediments (Figs. 10A-B. Such faults show transpressive
462 dextral kinematics, compatible with faulting in the Neogene deposits (Fig. 10C).
463 Along the EFS, Quaternary faulting is documented both along the principal
464 displacement zone and along subsidiary, synthetic fault strands (Fig. 3). Along the prominent
465 E-W striking fault scarp that defines the geomorphic expression of the EFS (Fig. 8A),
466 Quaternary deposits are extensively affected by a set of sub-vertical joint arrays. Further to
467 the east, along the NW-SE fault systems that make up the transtensional trailing-end
468 imbricate fan of a major fault dextral segment to the north of the EFS, extensional and dextral
469 oblique-slip faults involve the Ng-GM deposits and the Quaternary alluvial cover (Fig. 3).
470 Evidence of Quaternary faulting is documented along an E-W striking minor fault strand. In
471 this area, E-W oriented sub-vertical faults cut through the gypsiferous Neogene units and into
472 the Quaternary alluvial deposits, displaying calcite slickenlines and small-scale drag folding,
473 compatible with dextral kinematics (Fig. 10D-E).
474
475 **AHe THERMOCHRONOMETRY**
476 The low closure temperature for the apatite (U+Th)/He system (65–70°C for typical
477 rates of cooling and grain sizes; Farley, 2000) makes it particularly useful for assessing the
478 ages of the late-stage deformation and exhumation history affecting the uppermost portions of
479 the crust, where brittle deformation and faulting predominates.
480 Samples from the basement units (n= 6) and basal Neogene deposits (Ng-C and Ng-
481 SSi units; n = 11) were collected for AHe thermochronometry along an approximate constant
482 elevation transect parallel to the KFF trace (mean altitude of 1070 m; Fig. 11). The samples
483 are from the sandstone portions of the Paleozoic and Mesozoic deposits and the Neogene

484 basal sandy intercalations of Cycle-1 and -2. The quantity and quality of apatite grains are
485 highly variable. In most of the samples, apatite grains appear as rounded with frosted
486 surfaces, making the identification of inclusion-free grains difficult. Consequently, eight
487 samples were excluded from the analysis due to their poor apatite quality (Fig. 11).

488 The analytical protocol adopted in this study follows Foeken et al. (2006; 2007). Refer
489 to Appendix for methods and analytical procedure. Single grain ages corrected for α-ejection
490 (Farley et al., 1996) generally show a good within-sample reproducibility (Table 1). Mean
491 ages and standard deviations are plotted in Figure 11.Three samples show single grain ages
492 that does not overlap within two standard deviations with the other ages of the same sample.
493 Because these three grains have low U and Th content, we consider them as outliers and they
494 were not included in the mean age calculation. All samples have mean and single grain AHe
495 ages that are younger than the stratigraphic age, indicating that all were reset. The ages
496 indicate a Miocene to Pliocene cooling/exhumation history. Mean ages range from 2.9 ± 1.5
497 Ma to 20 ± 2.6 Ma, and define two mean age populations, clustering at ~18 and ~4 Ma (Table
498 1).

499 The spatial distribution of the AHe ages shows two broad areas: (i) the western area,
500 comprising the topographically prominent fault bounded basement high to the west of the
501 EFS, where cooling ages are older; and (ii) the eastern area, located alongside of the EFS,
502 where cooling ages are younger (Fig. 11). The AHe age distribution in the western area
503 shows that the basement bedrocks experienced a similar exhumation and cooling history
504 during and since the early Miocene, ~18 Ma, with the exception of sample IR-10, which
505 exhibits a cooling age of ~3 Ma. The AHe ages from the eastern area are systematically
506 younger, clustering at ~4 Ma. This pattern is not uniform, as sample IR-17, from the pre-
507 Neogene basement, shows an age of ~8 Ma. The distribution of AHe ages indicates a pattern
508 that may relate to differential exhumation/cooling history along the strike of the KFF.

509

510 **DISCUSSION**

511 The multidisciplinary dataset presented in this study gives spatial and temporal
512 constraints on the geological history and evolution of the KFF system (Fig. 1). By linking
513 structures, stratigraphy and apatite thermocronometry to the long-term response to crustal
514 deformation in intraplate settings the results may elucidate the way strike-slip faulting
515 nucleates and propagates.

516

517 **Structural synthesis**

518 The geological investigation shows that the KFF consists of three main, left stepping,
519 dextral fault strands that cut through the Paleozoic and Mesozoic basement units and the
520 Neogene-Quaternary sedimentary covers (Fig. 3). The fault zones are tens of kilometers long
521 and cut at high angle the NE-SW striking planar fabrics of the basement rocks (Fig. 3), ruling
522 out a major contribution of tectonic reactivation during the KFF development.

523 The dextral fault population (261 of 501 data) provides a mean strike cluster at N91°.
524 This is interpreted as the strike of the principal displacement zone (PDZ) of the KFF. The
525 normal faults and extensional veins strike data (n = 111) have strike clustering at N135°.
526 These angular relationships suggest fault zone development in response to a (local) regional
527 direction of the maximum principal stress ($R\sigma_1$) trending NW-SE, at an angle of ~44° from
528 the PDZ. This implies simple shear dominated strike-slip deformation (simple shear
529 wrenching in Fossen et al.,1994) during the KFF development, in agreement with the mean
530 pitch angle (2°) of the fault slickenlines as obtained from the cumulative fault data set (see
531 Fig. 3). Within this scenario, the along-strike spatial variation of the fault orientations,
532 kinematics and strain regimes (restraining and releasing areas) reflect the different ways by

533 which the overall E-W right lateral shear is accommodated, distributed and partitioned along
534 the principal and minor fault strands of the KFF system (Fig. 3).

535 Fault zone geometry and structural characteristics vary along-strike. There is an
536 eastward increase in shear localization within the main fault zones, from distributed
537 deformation characterized by cataclastic fault rocks in the west (the WFS and CFS) to
538 localized and mature fault zones characterized by ultracataclastic fault gouges (distributed
539 cataclastic flow) and S-C fabrics in the east (the EFS). Porous rocks such those that make up
540 the basal deposits of the faulted Neogene strata along the KFF, display a transition from
541 dilatant, brittle behaviour to shear-enhanced compaction and macroscopically ductile
542 behaviour with increasing effective pressure at constant temperature (Rutter and Hadizadeh,
543 1991; Scholz, 2002; Paterson et al., 2005; Wong and Baud, 2012). This is documented along
544 the KFF by the eastward variation of deformation mechanisms from brittle fracturing to
545 coupled cataclastic flow and dissolution creep during S-C fabric development. This is in
546 agreement with occurrence of hematite-coated fault surfaces systematically observed on the
547 EFS (Fig. 8c and d), which attests to focused fluid flow during fault zone localisation, a
548 process that does not occur at shallow (< 3 km) crustal depths (Caine et al., 1996; Rowland
549 and Sibson, 2004; Sheldon et al., 2006). Faulting was also intimately associated with regional
550 bulging (anticlinal folding) of the Neogene deposits (Fig. 3), providing further constrains on
551 the KFF growth and evolution. Folding is in fact better preserved in the west (cross sections
552 A-B and C-F in Fig. 3), while it dies out eastward, where it is abruptly interrupted by the EFS
553 (Fig. 3). It is inferred that folding was caused by the dilatant behaviour during initial
554 fracturing of the Neogene deposits. Folding was then amplified by fault zone propagation
555 (fault-related folding; both vertically and along-strike) in the Neogene deposits. With
556 increasing shearing, deformation zones matured into discrete through-going fault zones,
557 which localized deformation, preventing further fold amplification.

Such evidence suggests shear deformation occurred under different confining pressure conditions at different locations along the KFF, causing transition from diffuse to localised shear deformation moving eastward along the fault. Differential lithostatic loading between the western and the eastern areas is supported by the stratigraphic and thermochronometric data (see below), which shows an overall eastward increase in the Neogene sediment thickness (up to ~ 4 km) and fault-related exhumation post-dating Neogene sedimentation.

Estimation of the fault offset along the KFF is hampered by the lack of homologous markers cut by the major fault strands. Nevertheless, an indication of the magnitude of the horizontal separation along the fault strands that make up the KFF can be derived from the basement outcrop pattern across the NW-SE striking trace of the EFS. The basement block to the north of the EFS is in fact inferred to have been displaced south-eastward from its original position. In this scenario, a horizontal displacement of ~ 8 km can be proposed (Fig. 3). Further estimates can be obtained from empirically-derived scaling law for faults, relating fault displacement (D) to fault length (L), fault damage zone (DT) and fault core (CT) thickness (e.g. Fossen, 2010), respectively. Based on the field observation, the D-L diagram provides displacement values ranging from 10^2 to 10^3 m, which are in the range of those obtained from the DT-D and CT-D diagrams. Based on these estimates, it is therefore plausible to assume that the cumulative displacement accumulated along the dextral KFF deformation zone would be in the order of a few ten kilometers.

Neogene stratigraphy: linking faulting with sedimentation

The Neogene deposits associated with the KFF consist of a fining-upward succession, which is arranged in three main sedimentary cycles. The field observations document a progressive up-section decline in syn-depositional tilting, recorded by the gradual disappearance of progressive angular unconformities, coupled with a gradual waning of

583 synsedimentary faulting from Cycle-1 to the base of Cycle-3 (Figs 5a-c and 7d). The
584 presence of syn-sedimentary faulting, together with the overall syn-depositional geometry of
585 the Neogene deposits indicate that their deposition and tilting were controlled by localized
586 uplift along the KFF system and suggest fault-related topographic growth during the fault
587 system propagation. In such a scenario, the texturally immature and proximally-sourced
588 breccias and conglomerates of Cycle-1, are the stratigraphic marker of the growing linear
589 topography associated with KFF development. Furthermore, the Neogene deposits show
590 variation in facies distribution and thicknesses along-strike of the KFF. In particular, the
591 lower portion of Cycle-1, consisting of talus breccias (unit Ng-B), is only present in the
592 western areas (WFS and CFS) with greatest preserved thicknesses documented along the
593 central WFS (Fig. 3). This indicates that the fault-related topographic high, from which the
594 breccias were sourced, was initially confined to the western region. The greatest thickness of
595 talus breccias along the WFS (Figs. 3 and 5) indicates that the southern side of the KFF
596 experienced greater sediment supply influx and/or greater accommodation space. Also the
597 upper unit of Cycle-3 deposits is the thickest (constituting more than half of the total
598 Neogene stratigraphic succession) and the most laterally continuous. Its thickness, lateral
599 stratigraphic continuity, and lack of synsedimentary deformation, indicate that it was
600 deposited during a period of tectonic quiescence and most probably of regional subsidence.
601 Lastly, the KFF Neogene stratigraphic succession and the along-strike changes in
602 sedimentary facies, depositional patterns and thicknesses reflect a history of sedimentary
603 basins strongly influenced by tectonics and regulated by regional and local environmental
604 changes. The eastward increase in the thickness of the Neogene deposits may reflect a
605 migrating depocenter, controlled by the eastward propagation and evolution of the KFF
606 during the Neogene.
607

608 **A two-stage exhumation history**

609 The AHe thermochronometric data set defines two mean age populations, clustering at
610 ~18 and ~4 Ma. The early Miocene exhumation episode is recorded by basement samples
611 IR5, IR8 and IR15, that are located along the southwestern and central zones of the KFF. The
612 early Pliocene exhumation episode is chiefly recorded from the Neogene deposits along the
613 EFS (Fig. 11).

614 This early Miocene episode is interpreted as the beginning of faulting, topographic
615 growth and exhumation along the KFF. A source-to-sink scenario is inferred for this time
616 period, when the fault-related topographic growth caused the synchronous
617 erosion/exhumation of the topographically prominent basement units and deposition of the
618 eroded material in the surrounding lowland depocenter. This is supported by (i) the proximal
619 nature of the basal Ng-C conglomerates; (ii) the presence of progressively angular
620 unconformities in the basal portion of the Neogene sedimentary successions (Cycle-1 and -2);
621 and (iii) the bedding steepness that gradually decreases away from the boundary fault of the
622 fault systems and up section.

623 The fact that Neogene sediments from the EFS show AHe ages younger than their
624 source rocks indicate that they have been thermally reset. The reconstructed Neogene
625 stratigraphy indicates that the succession is up to ~4 km thick (Fig. 4), well above the
626 thickness needed to reset the AHe system at the base of the succession in a normal
627 continental geothermal setting (25-30 °C/km; Chapman, 1986). It is therefore inferred that
628 with the exception of the western and central area of the KFF zone (samples IR-5, IR-8 and
629 IR-15 in Fig. 11), the thickness of these Neogene deposits was sufficient to reset the
630 (U+Th)/He system of the detrital apatite in both the pre-Neogene and the basal Neogene
631 successions. In these areas, a renewed fault activity and fault-related exhumation occurred at
632 ~4Ma. This exhumation episode is further documented by the northward and southward post-

633 depositional tilting of the Neogene units, particularly the Ng-GM deposits. This event was
634 characterized by widespread erosion that preferentially targeted the lithologically weaker
635 Cycle-3 marls. In contrast to the first event, there is no stratigraphic record documenting the
636 topographic growth and general unroofing along the KFF. A major erosional unconformity
637 marks the contact between Neogene and Quaternary deposits. Sample IR-18 exhibits an
638 average age that lies between the two mean age clusters. This may reflect partial resetting.
639 Finally, the occurrence of the second exhumation episode along the KFF shows that the
640 topmost Neogene successions must be older than 4 Ma. This is compatible with a
641 stratigraphic position equivalent to that of the Upper Red Formation.
642 The KFF experienced a punctuated history of fault-related exhumation. The first fault-
643 related exhumation event started at ~18 Ma and progressively waned to a period of relative
644 tectonic quiescence and generalized subsidence during deposition of Cycle-3, some time
645 before ~4 Ma. This time period probably corresponds with the time when syn-sedimentary
646 faulting and tilting ended (mainly during the deposition of the Cycle-3 Ng-GM deposits). In
647 the absence of any age constraint on the Neogene stratigraphy, the exhumation rate associated
648 to the first exhumation episode can not be estimated.
649 The second exhumation event started during the early Pliocene (~4Ma) and is
650 probably responsible for the present structural architecture of the KFF. For each sample that
651 records the early Pliocene event, AHe ages were converted to exhumation rates using a
652 typical continental geothermal gradient of 25°C/km (e.g. Chapman, 1986), with a long-term
653 averaged annual surface temperature of 16°C (http://en.climate-data.org/location/5127/) and a
654 closure temperature of 70°C. Accordingly, the depth of the base of the apatite partial
655 retention zone prior to the onset of denudation must be ~2.1 km. Assuming that the closure
656 isotherms are roughly parallel to local mean elevation and taking into consideration that
657 samples were collected from approximately the same mean elevation at each location,

exhumation rates were not adjusted for local sample elevation. The calculated exhumation rates vary between 0.4 and 0.7 km/Ma, with a mean exhumation rate of 0.5 km/Ma. These exhumation rates are comparable with those obtained for the Alborz (0.2-0.7 km/Ma; Axen et al., 2001; Ballato et al., 2013), and the Zagros (~ 0.2-0.6 km/Ma; Mouthereau, 2011), for the same time frame.

The long-term evolution: fault nucleation, propagation and growth

Analogue modeling studies have shown that strike-slip fault systems nucleate and evolve from distributed to localized, through-going fault strands (for review see Dooley and Schreurs, 2012). On the assumption that the topographic evolution and stratigraphic response was structurally controlled during the documented two-stage history of fault zone development, a five-step model is proposed for the long-term evolution of the KFF (Fig. 12). (i) **Fault system nucleation**. The fault nucleation stage is attested by the initial topographic growth and basement exhumation, in a scenario of diffuse deformation at ~18 Ma (Fig. 12a). Topographic growth is inferred to have been achieved by a combination of: (a) transpressive regimes (e.g. Woodcock and Rickards, 2003; Cunningham, 2013), (b) structural irregularities such as stepovers (Aydin and Nur, 1985; Hilley and Arrowsmith, 2008; Finzi et al., 2009; Carne and Little, 2012), (c) local variations in master fault dip (Dair and Cooke, 2009), and (d) pervasive, tectonically-induced fracturing and associated volume increase (5 to 10%; Braun, 1994; Schopfer and Steyrer, 2001; Le Guerroué and Cobbold, 2006; Schrank and Cruden, 2010). The net result of these processes operating together and over different spatial and temporal scales was the growth of a topographically prominent bulge along the evolving fault zone (Fig. 12A). In the absence of well-developed drainage networks the eroded material was mainly mobilized by gravity-driven processes and deposited into the adjacent

682 basins as thick packages of proximally-sourced breccias at the base of the Neogene Cycle-1
683 (Ng-B and -C).
684 (ii) ***Fault localization and propagation***. Faulting was probably initially accommodated by a
685 network of distributed en-echelon Riedel shears that successively merged by sideways
686 propagation or linkage to form through-going master faults (Fig. 12B). In this context, due to
687 the strain hardening and velocity-strengthening properties of poorly consolidated syn-tectonic
688 sediments (e.g. Scholz, 2002), fault propagation was probably inhibited within the newly
689 deposited material. This had the effect of favoring faulting along areas free of unconsolidated
690 sediments, causing faulting activity to migrate inwards, gradually localizing along sub-
691 vertical fault zones at the basement-sediment interface (Le Guerroué and Cobbold, 2006; Fig.
692 12B). The positive feedback among topographic growth, erosion, sedimentation and inward
693 fault migration is the primary driver for the progressive narrowing of the fault system and of
694 the associated topographic growth. As a result, syn-sedimentary faulting accompanied the
695 topographic growth and the progressive tilting of the deposits. The drainage network
696 developed further as deformation continued, creating larger catchments capable of producing
697 yet more texturally mature sediments. Such conditions produced proximal alluvial fans
698 deposits consisting of gravelly sandstones, intermediate alluvial plains consisting of
699 clinostratified and cross-bedded channel fill and bar sandstones deposits, which distally
700 evolve into fluvio-palustrine facies (Neogene Cycle-2 deposits). Distribution of the Cycle-2
701 deposits indicates increasing thicknesses towards the NE, suggesting preferred sediment
702 influx/rooting towards this region (Fig. 12B).
703 (iii) **Fault termination**. Development of trailing extensional imbricate fan terminations at the
704 eastern fault tips (Woodcock and Fischer, 1986; Figs. 3 and 12C) attests to strike-slip shear
705 dissipation at fault zone terminations. The extensional/transtensional faulting and the
706 associated fault-controlled depocenters (cf. Wu et al., 2009) developed at the same time as

707 deposition of the basal part of the Neogene Cycle-3 (Ng-GM deposits). Their distribution and
708 the syn-tectonic character of its deposition allow us to define the distribution and geometries
709 of the subsiding areas and basin boundary faults (Fig. 12C).
710 (iv) **Tectonic quiescence**. Tectonic activity progressively waned during the deposition of unit
711 Ng-GM, as attested by the gradual up-section disappearance of syn-sedimentary faulting and
712 tilting. The Cycle-3 Ng-MS deposits progressively covered the entire KFF area. Their
713 thickness, lateral stratigraphic continuity and lack of syn-sedimentary deformation indicate
714 that they were deposited during a period of tectonic quiescence and, most probably, of
715 regional subsidence (Fig. 12D).
716 (v) **Renewed Faulting.** Deformation and faulting activity resumed at ~4Ma, reactivating
717 most of the pre-existing faults strands and creating new ones that propagated further eastward
718 (Fig. 12E). This renewed fault activity is considered to be responsible for the current fault
719 zone geometry, developed in a regime of simple shear dominated strike-slip faulting. It
720 affected a heterogeneous upper crustal section, as due to the anisotropic distribution of the
721 Neogene deposits. To the east, where higher confining pressure was provided by the thick
722 Neogene sediments (up to 4 km in thickness), combined cataclastic flow and dissolution
723 creep allowed mature fault zones to develop. To the west, the reduced confining pressure
724 means the fault zone was less localized and characterized by dilatant brittle behaviour of the
725 Neogene deposits, associated with volume increase accommodated by the regional anticlinal
726 folding of the Neogene deposits (Fig. 3). In the western area, topographic growth was also
727 achieved by the left-stepping geometry between the dextral WFS and the CFS (Fig. 3). The
728 eastward propagation of the KFF system prevented further fold amplification, with a
729 progressive localization of strain under higher confining pressure conditions.
730 The renewed topographic growth along the KFF was accompanied by widespread
731 erosion and unroofing (Fig. 12E). The fact that no syn-tectonic deposits are preserved in the

proximity (tens of kilometres) of the KFF during this second event suggests that it was accompanied by an erosional phase, as also testified by a regional pediment cutting the tilted Neogene deposits, during which time the eroded material could get efficiently transported away from the KFF area.

During the Late Pleistocene and Holocene new, climate-driven, aggradation phases took place as testified by the different generations of alluvial fans and fluvial terraces widely recognized in eastern Iran (Regard et al., 2006; Fattahi et al., 2007; Walker and Fattahi, 2011; Foroutan et al., 2014). Evidence of dextral transpressional shear affecting these Quaternary alluvial deposits along the KFF system suggests that the transpressional regime renewed and is probably still active along the KFF, being responsible for the present topography of the KFF deformation zone.

From the above scenario, assuming that renewed faulting started at ~4 Ma and continued at a constant rate, estimates of the slip rates based on the estimated horizontal apparent displacement (~8 km) along the KKF fault strands (EFS) are in the range of ~2 mm/yr. The calculated slip rate is comparable with those obtained for the E-W oriented strike-slip Doruneh Fault ranging from 1.3-2.5 mm/yr (Fattahi et al., 2007; Farbod et al., 2011; Walpersdorf et al., 2014) and Dasht-e-Bayaz fault ranging from 1-2.5 mm/yr (Berberian and Yeats, 1999; Walker et al., 2004).

Regional implications

The early Miocene tectonic/exhumation event recognized along the KFF is in good agreement with the regional thermochronometric results, as obtained from the Zagros, Alborz and Talesh areas (Khadivi et al., 2012; Ballato et al., 2013; Madanipour et al., 2013). It also correlates with the late-stage, early Miocene exhumation of the Kashmar-Kerman Tectonic Zone (Fig. 1), which is interpreted as the transition from extensional to compressional

757 tectonics in the region (Verdel et al., 2007). Within this context, the reconstructed source-to-
758 sink scenario along the KFF places onset of deposition of Neogene continental successions of
759 the Upper Red Formation in Central Iran at the early Miocene. This age is compatible with
760 the Burdigalian-Messinian age of the Upper Red Formation (Ballato et al., 2008), but
761 contrasts with the recently proposed Burdigalian-Serravallian age for the "e" member of the
762 Qom Formation (Hadavi et al., 2010), which instead implies a possible post-Serravallian
763 onset of the continental deposition of the Upper Red Formation. This suggests a diachronic
764 distribution of the Neogene continental deposits and a controlling mechanism operated by
765 regional tectonics on the Neogene sedimentary facies distribution and stratigraphy in Central
766 Iran.

767 The early Pliocene event is coeval with a regional tectonic reorganization, as inferred
768 from the recognized acceleration in uplift rates in the Alborz and Talesh mountains and by
769 fault kinematic changes in the Kopeh Dagh and along the Zagros-Makran Transfer zone
770 (Axen et al., 2001; Regard et al., 2005; Shabanian et al., 2009a; Hollingsworth et al., 2010;
771 Rezaeian et al., 2012; Madanipour et al., 2013; Robert et al., 2014). The Miocene-Pliocene
772 boundary also corresponds with the time when the Zagros collisional zone became
773 overthickened to sustain further shortening (Allen et al., 2004; Austermann and Iaffaldano,
774 2013).

775 The cause of the Pliocene regional tectonic event across the Iranian plateau is still
776 uncertain, with several geodynamic/tectonic scenarios proposed so far: (i) onset of subduction
777 in the South Caspian Basin (Jackson et al., 2002; Mothreau et al., 2012; Madanipour et al,
778 2013); (ii) a switch from westward/northwestwards to northeastward escape of Central Iran,
779 triggered by the Afghan and western margin of the Indian collision, sealing off a free face at
780 the eastern side of the Arabia–Eurasia collision zone (Allen et al., 2011); and (iii) activation

781 of the Zagros-Makran transfer zone between the collision domain and the Makran subduction
782 domain (eastern Iran) (Regard et al., 2010).
783 Regardless of the ultimate cause of the Pliocene event, our AHe age data constitute
784 the first direct documentation of such an event in Central Iran. Therefore, a reappraisal of the
785 Neogene-Quaternary space-time kinematic evolution and fault distribution within Central
786 Iran is needed. In particular, the following evidence is not compatible with the kinematic
787 configuration and rigid block rotation model proposed for central Iran: (i) fault zone
788 (re)activation and kinematic shifts punctuated in time and space at the northern edge of the
789 Lut block during Neogene-Quaternary (Javadi et al., 2013; Nozaem et al., 2013; this study);
790 and (ii) Neogene-Quaternary NW-SE to E-W dextral strike-slip kinematics acting at rates
791 compatible with the regional average values along the northern edge of the Lut Block to the
792 south of the Doruneh Fault (cfr. Allen et al., 2004; 2011; Walker and Jackson, 2004; Mattei et
793 al., 2012; Walpersdorf et al., 2014).
794 We tentatively propose that the Neogene-Quaternary deformation in the Iranian
795 plateau has been primarily controlled by the spatial and temporal variations in the degree of
796 tectonic coupling along the Arabia-Eurasia collision interface, in the framework of a constant
797 N-S directed convergence velocity scenario (McQuarrie and van Hinsbergen, 2013). Indeed,
798 the along-strike variation from continent-continent convergence in the Zagros to ocean-
799 continent convergence in the Makran and, hence, from a fully to a partially coupled
800 collisional boundary (Fig. 1), might have imposed a northeastward escape component to the
801 intraplate domain (Regard et al., 2010) with polycyclic reactivation of the Kashmar-Kerman
802 Tectonic Zone along the Kuh-e-Sarhangi, Kuh-e-Faghan and Doruneh fault strands (Verdel et
803 al., 2007; Javadi et al., 2013; Nozaem et al., 2013; this study). In this scenario, the N-S
804 dextral strike-slip faults at the edges of the CEIM may have accommodated the differential
805 displacement between the collision domain of Central Iran and the Makran subduction

806 domain of Eastern Iran. This has been occurring between non rotating blocks such as between
807 Central and Eastern Iran (Deshir and Anar faults (Fig. 1); Meyer and Le Dortz, 2007).
808
809 **Implications for topographic growth along intraplate strike-slip faults**
810 Integration of the multidisciplinary data-set presented in this study results in a model for
811 long-term, spatially and temporally punctuated fault system evolution. Based on the regional
812 scenario and synchronicity with the regional deformation events leading to the growth of the
813 Iranian Plateau, the reason for the nonlinear temporal evolution of intraplate faulting is
814 partially attributable to changes in the regional (far field) stress regime through time.
815 Tectonic stresses are generated at the plate margins and are transferred to the intraplate
816 domains, where they interact with pre-existing structures and local (near-field) kinematically-
817 induced stress regimes.
818 Several other factors influence deformation in the near-field at the scale of the developing
819 fault system, such as spatial changes in the degree of fault development maturity and
820 structural complexity during fault development. The spatial-temporal changes in those
821 interactions and feedbacks regulate the way plate boundary stresses are transferred to the
822 intraplate domains and may ultimately be responsible for the punctuated development of
823 intraplate deformation and associated topographic growth. In particular, the study recognizes
824 that the positive feedback among topographic growth, erosion, sedimentation and inward
825 fault migration is the primary driver for the progressive fault zone localization, narrowing of
826 the fault system and of its topographic growth.
827
828 **CONCLUSIONS**
829 The main results of this study are as follows:

(i) The KFF consists of a major E-W striking, 80 km long dextral strike-slip brittle deformation zone, made up of three broadly left stepping, E-W striking, dextral, strike-slip fault strands, which cut through the Neogene sedimentary cover and the unconformably overlying Quaternary deposits.

(ii) The KFF is characterized by simple shear dominated dextral strike-slip deformation. The along-strike spatial variation of the fault orientations, kinematics and strain regimes (restraining and releasing areas) reflect the different ways by which the overall E-W right lateral shear is accommodated, distributed and partitioned along the principal and minor fault strands of the KFF system.

(iii) AHe thermochronometry indicates the KFF system propagation was punctuated in time and space, and associated with two major episodes of fault-related exhumation, at ~18 Ma (Early Miocene) and ~4 Ma (Early Pliocene).

(iv) The stratigraphic, structural and thermochronometric datasets shows that the KFF nucleated in the west and propagated eastward in two punctuated events.

(v) The first faulting/exhumation episode is chiefly recorded by the structure and deposition of the Neogene deposits along the KFF, where a source-to-sink scenario can be reconstructed for this time frame, when topographic growth caused the synchronous erosion/exhumation of the pre-Neogene units and deposition of the eroded material in the surrounding fault-bounded continental depocenters.

(vi) The KFF gradually entered a period of relative tectonic quiescence and, probably, regional subsidence during which a thick pile of fine-grained onlapping sediments were deposited, and caused the resetting of the (U+Th)/He system of the detrital apatite grains hosted both within the pre-Neogene and the basal Neogene successions. The second faulting episode at ~4 Ma, recorded by the AHe ages and

by the further tilting of the Neogene deposits, caused the final exhumation of the fault system, resulting in the current fault zone geometry and topography.

(vii) The two fault-related exhumation events are nearly coincident with (1) the well documented acceleration of collision-related uplift in the early Miocene along the Arabia-Eurasia collision zone, and (2) the inferred early Pliocene tectonic reorganization of central Iran.

Results from this study suggest that the intraplate deformation zones are particularly sensitive to major tectonic changes occurring at the plate boundaries (far-field effects), and, as such, they can be regarded as a gauge for plate-tectonics induced state of stress changes at the plate boundaries. The results also suggest that the propagation and evolution of intraplate strike-slip fault systems is accompanied by substantial topographic growth, exhumation, erosion and production of syn-tectonic deposits, whose distribution, geometry and facies characteristics are strongly influenced by the spatio-temporal propagation history and structural evolution of the fault system (near field effects).

ACKNOWLEDGMENTS

Special thanks go to M.R. Mazinani for assistance during field work. The manager and staff of Khanyeh-e-Moallem of Kashmar are warmly thanked for their kind hospitality. We also thank Ali Rastpour and Hassan Faraji for driving to the field and logistic support. F. Salvini is thanked for his advice during fault population analysis. Constructive reviews by F. Mouthreau and D. Peacock significantly contributed to improve the final version of the manuscript. This project has been funded by TOPOMOD Marie Curie ITN project (Grant agreement 264517).

APPENDIX A: (U-TH)/He THERMOCHRONOMETRY

(U-Th)/He thermochronometry is based on the ingrowth of a particles (He) produced mainly by U and Th decay. The He diffusivity within the crystal lattice is a function primarily of temperature and in minor way of grains size and distribution of parent isotope (Ehlers and Farley, 2003). Helium diffusive loss is complete in typical apatites at temperatures in excess of ~75°C, it becomes limited between ~75°C and ~40°C, an interval called partial retention zone (HePRZ) (House et al., 1999; Farley, 2000). Assuming no other source for the He, the measured He age records the time the rock cooled below the closure temperature of ~70°C. Inclusion-free apatite for (U-Th)/He analysis were hand-picked under a high-magnification binocular microscope with cross-polarized light. Single crystals were packed into Pt foil capsules. 3 to 5 apatite grains were analyzed for each sample. Helium was extracted by heating the Pt-tubes at 600–700°C for 1–2 min using a laser diode following the procedures described by Foeken et al. (2006). ^{4}He concentrations were measured by comparison to a calibrated standard 4He using a Hiden HAL3F quadrupole mass spectrometer equipped with an electron multiplier. The accuracy of measurements was checked by repeated measurements of an in-house He standard. System blank levels were trivial in comparison to measured He abundances and no correction was necessary. Apatites were then dissolved in 5% HNO_3 with ^{235}U and ^{230}Th spikes and measured by VG Plasma Quad 2 ICP-MS. Correction for He recoil loss (Ft) was made using conventional procedure (Farley et al., 1996).

899 **REFERENCES**

900 Agard, P., Omrani, J., Jolivet, L., Whitechurch, H., Vrielynck, B., Spakman, W., Monié, P.,
901 Meyer, B., and Wortel, R., 2011, Zagros orogeny: a subduction-dominated process:
902 Geological Magazine, v. 148, p. 692-725, doi: 10.1017/S001675681100046X.

903 Aghanabati, A., 2004, Geology of Iran, Geological Survey of Iran, Tehran, 582 p.

904 Aitken, A. R. A., Raimondo, T., and Capitanio, F. A., 2013, The intraplate character of
905 supercontinent tectonics: Gondwana Research, v. 24, p. 807-814, doi:
906 10.1016/j.gr.2013.03.005.

907 Allen, M., Jackson, J., and Walker, R., 2004, Late Cenozoic reorganization of the Arabia-
908 Eurasia collision and the comparison of short-term and long-term deformation rates:
909 Tectonics, v. 23, TC2008, doi: 10.1029/2003tc001530.

910 Allen, M. B., and Armstrong, H. A., 2008, Arabia–Eurasia collision and the forcing of mid-
911 Cenozoic global cooling: Palaeogeography, Palaeoclimatology, Palaeoecology, v. 265,
912 p. 52-58, doi: 10.1016/j.palaeo.2008.04.021.

913 Allen, M. B., Kheirkhah, M., Emami, M. H., and Jones, S. J., 2011, Right-lateral shear across
914 Iran and kinematic change in the Arabia—Eurasia collision zone: Geophysical Journal
915 International, v. 184, no. 2, p. 555-574, doi: 10.1111/j.1365-246X.2010.04874.x.

916 Amini, A., 1997, Provenance and depositional environment of the Upper Red Formation,
917 central zone Iran [Ph.D. thesis]: The University of Manchester.

918 Austermann, J., and Iaffaldano, G., 2013, The role of the Zagros orogeny in slowing down
919 Arabia-Eurasia convergence since ~5 Ma: Tectonics, v. 32, p. 351-363, doi:
920 10.1002/tect.20027.

921 Avouac, J.-P., Ayoub, F., Wei, S., Ampuero, J.-P., Meng, L., Leprince, S., Jolivet, R.,
922 Duputel, Z., and Helmberger, D., 2014, The 2013, Mw 7.7 Balochistan earthquake,

energetic strike-slip reactivation of a thrust fault: Earth and Planetary Science Letters, v. 391, p. 128-134, doi: 10.1016/j.epsl.2014.01.036.

Axen, G. J., Lam, P. S., Grove, M., Stockli, D. F., and Hassanzadeh, J., 2001, Exhumation of the west-central Alborz Mountains, Iran, Caspian subsidence, and collision-related tectonics: Geology, v. 29, p. 559-562, doi: 10.1130/0091.

Aydin, A., Nur, A. 1985, The types and role of stepovers in strike-slip tectonics, *in*: Biddle K. T., Christie-Blick N. eds., Strike-Slip Deformation, Basin Formation, and Sedimentation: The Society of Economic Paleontologists and Mineralogists, Special Publication, v. 37, p. 35–45.

Ballato, P., Nowaczyk, N. R., Landgraf, A., Strecker, M. R., Friedrich, A., and Tabatabaei, S. H., 2008, Tectonic control on sedimentary facies pattern and sediment accumulation rates in the Miocene foreland basin of the southern Alborz mountains, northern Iran: Tectonics, v. 27, TC6001, doi: 10.1029/2008tc002278.

Ballato, P., Uba, C. E., Landgraf, A., Strecker, M. R., Sudo, M., Stockli, D. F., Friedrich, A., and Tabatabaei, S. H., 2011, Arabia-Eurasia continental collision: Insights from late Tertiary foreland-basin evolution in the Alborz Mountains, northern Iran: Geological Society of America Bulletin, v. 123, p. 106-131, doi: 10.1130/b30091.1.

Ballato, P., Stockli, D. F., Ghassemi, M. R., Landgraf, A., Strecker, M. R., Hassanzadeh, J., Friedrich, A., and Tabatabaei, S. H., 2013, Accommodation of transpressional strain in the Arabia-Eurasia collision zone: new constraints from (U-Th)/He thermochronology in the Alborz mountains, north Iran: Tectonics, v. 32, p. 1-18, doi: 10.1029/2012tc003159.

Bayasgalan, A., Jackson, J., Ritz, J.-F., and Carretier, S., 1999, `Forebergs', flower structures, and the development of large intra-continental strike-slip faults: the Gurvan Bogd fault

947 system in Mongolia: Journal of Structural Geology, v. 21, p. 1285-1302, doi:
948 10.1016/S0191-8141(99)00064-4.
949 Behroozi, A., Sahbaei, M., Etemadi, N., Zedeh, A. A., Ghomashi, A., and Moghtader, M.,
950 1987, Geological Map of Feyz Abad: Geological Survey of Iran, scale 1:100000,
951 Teheran, Iran.
952 Berberian, M., 1974, A brief geological descriptionof north-central Iran, in, Tchalenko J.S.,
953 Ambraseys N.N., Berberian M., Iranmanesh M.H., Mohajer-Ashjai A., Bailly M. and
954 Arsovsky M., eds., Materials for the Study of the Seismotectonics of Iran, North-
955 Central Iran: Geological Survey of Iran Report 29, p. 127–138.
956 Berberian, M., 2014, Earthquakes and Coseismic Surface Faulting on the Iranian Plateau:
957 Oxford, Elsevier Science, 776 p.
958 Berberian, M., and King, G. C. P., 1981, Towards a paleogeography and tectonic evolution of
959 Iran: Canadian Journal of Earth Sciences, v. 18, no. 2, p. 210-265, doi: 10.1139/e81-
960 019.
961 Berberian, M., and Yeats, R. S., 1999, Patterns of historical earthquake rupture in the Iranian
962 Plateau: Bulletin of the Seismological Society of America, v. 89, no. 1, p. 120-139.
963 Braun, J., 1994, Three-dimensional numerical simulations of crustal-scale wrenching using a
964 non-linear failure criterion: Journal of Structural Geology, v. 16, no. 8, p. 1173-1186,
965 doi: 10.1016/0191-8141(94)90060-4.
966 Buscher, J. T., and Spotila, J. A., 2007, Near-field response to transpression along the
967 southern San Andreas fault, based on exhumation of the northern San Gabriel
968 Mountains, southern California: Tectonics, v. 26, TC5004, doi: 10.1029/2006tc002017.
969 Caine, J. S., Evans, J. P., and Forster, C. B., 1996, Fault zone architecture and permeability
970 structure: Geology, v. 24, no. 11, p. 1025-1028, doi: 10.1130/0091-
971 7613(1996)024<1025:fzaaps>2.3.co;2.

Calais, E., Vergnolle, M., San'kov, V., Lukhnev, A., Miroshnitchenko, A., Amarjargal, S., and Déverchère, J., 2003, GPS measurements of crustal deformation in the Baikal-Mongolia area (1994–2002): Implications for current kinematics of Asia: Journal of Geophysical Research: Solid Earth, v. 108, no. B10, p. 2501, doi: 10.1029/2002jb002373.

Carne, R. C., and Little, T. A., 2012, Geometry and scale of fault segmentation and deformational bulging along an active oblique-slip fault (Wairarapa fault, New Zealand): Geological Society of America Bulletin, v. 124, no. 7-8, p. 1365-1381, doi: 10.1130/b30535.1.

Chapman, D. S., 1986, Thermal gradients in the continental crust: in Dawson, J.B., Carswell, D.A., Hall, J., and Wedepohl, K.H., eds., The Nature of the Lower Continental Crust: Geological Society, London, Special Publications, v. 24, no. 1, p. 63-70, doi: 10.1144/gsl.sp.1986.024.01.07.

Christie-Blick, N., and Biddle, K.T., 1985, Deformation and basin formation along strike-slip faults, in Biddle, K.T., and Christie-Blick, N., eds., Strike-Slip Deformation, Basin Formation, and Sedimentation: The Society of Economic Paleontologists and Mineralogist Special Publication 37, p. 1–34.

Cloetingh, S., Ziegler, P. A., Beekman, F., Andriessen, P. A. M., Matenco, L., Bada, G., Garcia-Castellanos, D., Hardebol, N., Dèzes, P., and Sokoutis, D., 2005, Lithospheric memory, state of stress and rheology: neotectonic controls on Europe's intraplate continental topography: Quaternary Science Reviews, v. 24, no. 3–4, p. 241-304, doi: 10.1016/j.quascirev.2004.06.015.

Cox, S. C., Stirling, M. W., Herman, F., Gerstenberger, M., and Ristau, J., 2012, Potentially active faults in the rapidly eroding landscape adjacent to the Alpine Fault, central Southern Alps, New Zealand: Tectonics, v. 31, TC2011, doi: 10.1029/2011tc003038.

997 Cunningham, D., 2013, Mountain building processes in intracontinental oblique deformation
998 belts: Lessons from the Gobi Corridor, Central Asia: Journal of Structural Geology, v.
999 46, p. 255-282, doi: 10.1016/j.jsg.2012.08.010.
1000 Cunningham, W. D., and Mann, P., 2007, Tectonics of strike-slip restraining and releasing
1001 bends: in Cunningham, W.D., and Mann, P., eds., Tectonics of Strike-Slip Restraining
1002 and Releasing Bends: Geological Society, London, Special Publications, v. 290, no. 1,
1003 p. 1-12, doi: 10.1144/sp290.1.
1004 Dair, L., and Cooke, M. L., 2009, San Andreas fault geometry through the San Gorgonio
1005 Pass, California: Geology, v. 37, no. 2, p. 119-122, doi: 10.1130/g25101a.1.
1006 Daneshian, J., and Dana, L. R., 2007, Early Miocene benthic foraminifera and biostratigraphy
1007 of the Qom Formation, Deh Namak, Central Iran: Journal of Asian Earth Sciences, v.
1008 29, no. 5–6, p. 844-858, doi: 10.1016/j.jseaes.2006.06.003.
1009 Di Vincenzo, G., Rossetti, F., Viti, C., and Balsamo, F., 2013, Constraining the timing of
1010 fault reactivation: Eocene coseismic slip along a Late Ordovician ductile shear zone
1011 (northern Victoria Land, Antarctica): Geological Society of America Bulletin, v. 125,
1012 no. 3-4, p. 609-624, doi: 10.1130/b30670.1.
1013 Doblas, M., 1998, Slickenside kinematic indicators: Tectonophysics, v. 295, no. 1–2, p. 187-
1014 197, doi: 10.1016/S0040-1951(98)00120-6.
1015 Dooley, T. P., and Schreurs, G., 2012, Analogue modelling of intraplate strike-slip tectonics:
1016 A review and new experimental results: Tectonophysics, v. 574–575, p. 1-71, doi:
1017 10.1016/j.tecto.2012.05.030.
1018 Dyksterhuis, S., and Müller, R. D., 2008, Cause and evolution of intraplate orogeny in
1019 Australia: Geology, v. 36, no. 6, p. 495-498, doi: 10.1130/g24536a.1.
1020 Eftekhar-Nezhad, J., Aghanabati, A., Hamzehpour, B., and Baroyant, V., 1976, Geological
1021 map of Kashmar: Geological Survey of Iran, scale 1:250000, Teheran, Iran.

1022 Ehlers, T.A., and Kenneth A. Farley, K.A., 2003, Apatite (U–Th)/He thermochronometry:
1023 methods and applications to problems in tectonic and surface processes: Earth and
1024 Planetary Science Letters, v. 206, p. 1-14.
1025 Ellis, S., 1996, Forces driving continental collision: Reconciling indentation and mantle
1026 subduction tectonics: Geology, v. 24, no. 8, p. 699-702, doi: 10.1130/0091-
1027 7613(1996)024<0699:fdccri>2.3.co;2.
1028 Farbod, Y., Bellier, O., Shabanian, E., and Abbassi, M. R., 2011, Geomorphic and structural
1029 variations along the Doruneh Fault System (central Iran): Tectonics, v. 30, no. 6,
1030 TC6014, doi: 10.1029/2011tc002889.
1031 Farley, K. A., 2000, Helium diffusion from apatite: General behavior as illustrated by
1032 Durango fluorapatite: Journal of Geophysical Research: Solid Earth, v. 105, no. B2, p.
1033 2903-2914, doi: 10.1029/1999jb900348.
1034 Farley, K. A., Wolf, R. A., and Silver, L. T., 1996, The effects of long alpha-stopping
1035 distances on (U-Th)/He ages: Geochimica et Cosmochimica Acta, v. 60, no. 21, p.
1036 4223-4229, doi: 10.1016/S0016-7037(96)00193-7.
1037 Fattahi, M., Walker, R. T., Khatib, M. M., Dolati, A., and Bahroudi, A., 2007, Slip-rate
1038 estimate and past earthquakes on the Doruneh fault, eastern Iran: Geophysical Journal
1039 International, v. 168, no. 2, p. 691-709, doi: 10.1111/j.1365-246X.2006.03248.x.
1040 Finzi, Y., Hearn, E., Ben-Zion, Y., and Lyakhovsky, V., 2009, Structural Properties and
1041 Deformation Patterns of Evolving Strike-slip Faults: Numerical Simulations
1042 Incorporating Damage Rheology: Pure and Applied Geophysics, v. 166, no. 10-11, p.
1043 1537-1573, doi: 10.1007/s00024-009-0522-1.
1044 Fitzgerald, P. G., Stump, E., and Redfield, T. F., 1993, Late Cenozoic Uplift of Denali and Its
1045 Relation to Relative Plate Motion and Fault Morphology: Science, v. 259, p. 497-499,
1046 doi: 10.1126/science.259.5094.497.

1047 Fitzgerald, P. G., Sorkhabi, R. B., Redfield, T. F., and Stump, E., 1995, Uplift and denudation
1048 of the central Alaska Range: A case study in the use of apatite fission track
1049 thermochronology to determine absolute uplift parameters: Journal of Geophysical
1050 Research: Solid Earth, v. 100, p. 20175-20191, doi: 10.1029/95jb02150.
1051 Foeken, J. P. T., Stuart, F. M., Dobson, K. J., Persano, C., and Vilbert, D., 2006, A diode
1052 laser system for heating minerals for (U-Th)/He chronometry: Geochemistry,
1053 Geophysics, Geosystems, v. 7, no. 4, doi: 10.1029/2005gc001190.
1054 Foeken, J. P. T., Persano, C., Stuart, F. M., and ter Voorde, M., 2007, Role of topography in
1055 isotherm perturbation: Apatite (U-Th)/He and fission track results from the Malta
1056 tunnel, Tauern Window, Austria: Tectonics, v. 26, no. 3, doi: 10.1029/2006tc002049.
1057 Foroutan, M., Meyer, B., Sébrier, M., Nazari, H., Murray, A. S., Le Dortz, K., Shokri, M. A.,
1058 Arnold, M., Aumaître, G., Bourlès, D., Keddadouche, K., Solaymani Azad, S., and
1059 Bolourchi, M. J., 2014, Late Pleistocene-Holocene right slip rate and paleoseismology
1060 of the Nayband fault, western margin of the Lut block, Iran: Journal of Geophysical
1061 Research: Solid Earth, v. 119, no. 4, doi: 10.1002/2013jb010746.
1062 Fossen, H., 2010, Structural geology, Cambridge University Press.
1063 Fossen, H., Tikoff, B., and Teyssier, C., 1994, Strain modeling of transpressional and
1064 transtensional deformation: Norsk Geologisk Tidsskrift, v. 74, no. 3, p. 134-145.
1065 Gavillot, Y., Axen, G. J., Stockli, D. F., Horton, B. K., and Fakhari, M. D., 2010, Timing of
1066 thrust activity in the High Zagros fold-thrust belt, Iran, from (U-Th)/He
1067 thermochronometry: Tectonics, v. 29, no. 4, doi: 10.1029/2009tc002484.
1068 Ghomashi, A., Masoomi, R., Hosseiny, S. Z., Taheri, J., Shamanian, G., Kaveh, N. S.,
1069 Baheremand, M., and Razavi, M. A., 2001, Geological Map of Kashmar: Geological
1070 Survey of Iran, scale 1:100000, Teheran, Iran.

1071 Granier, T., 1985, Origin, damping, and pattern of development of faults in granite:
1072 Tectonics, v. 4, no. 7, p. 721-737, doi: 10.1029/TC004i007p00721.
1073 Guest, B., Stockli, D. F., Grove, M., Axen, G. J., Lam, P. S., and Hassanzadeh, J., 2006,
1074 Thermal histories from the central Alborz Mountains, northern Iran: Implications for
1075 the spatial and temporal distribution of deformation in northern Iran: Geological
1076 Society of America Bulletin, v. 118, no. 11-12, p. 1507-1521, doi: 10.1130/b25819.1.
1077 Hadavi, F., Notghi Moghaddam, M., and Mousazadeh, H., 2010, Burdigalian–Serravalian
1078 calcareous nannoplanktons from Qom Formation, North-Center Iran: Arabian Journal
1079 of Geosciences, v. 3, no. 2, p. 133-139, doi: 10.1007/s12517-009-0052-2.
1080 Hafkenscheid, E., Wortel, M. J. R., and Spakman, W., 2006, Subduction history of the
1081 Tethyan region derived from seismic tomography and tectonic reconstructions: Journal
1082 of Geophysical Research: Solid Earth, v. 111, doi: 10.1029/2005jb003791.
1083 Hassami, K., Jamali, F., and Tabassi, H., 2003, Major active faults of Iran: International
1084 institute of earthquake engineering and seismology of Iran Press, scale 1:2,500,000..
1085 Hatzfeld, D., and Molnar, P., 2010, Comparisons of the kinematics and deep structures of the
1086 Zagros and Himalaya and of the Iranian and Tibetan plateaus and geodynamic
1087 implications: Reviews of Geophysics, v. 48, no. 2, doi: 10.1029/2009rg000304.
1088 Headley, R. M., Enkelmann, E., and Hallet, B., 2013, Examination of the interplay between
1089 glacial processes and exhumation in the Saint Elias Mountains, Alaska: Geosphere, v.
1090 9, no. 2, p. 229-241, doi: 10.1130/ges00810.1.
1091 Heidbach, O., Tingay, M., Barth, A., Reinecker, J., Kurfeß, D., and Müller, B., 2008, The
1092 World Stress Map database release 2008, doi: 10.1594/gfz: WSM. Rel2008.
1093 Hessami, K., Koyi, H. A., Talbot, C. J., Tabasi, H., and Shabanian, E., 2001, Progressive
1094 unconformities within an evolving foreland fold–thrust belt, Zagros Mountains: Journal
1095 of the Geological Society, v. 158, no. 6, p. 969-981, doi: 10.1144/0016-764901-007.

1096 Hilley, G. E., and Arrowsmith, J. R., 2008, Geomorphic response to uplift along the Dragon's
1097 Back pressure ridge, Carrizo Plain, California: Geology, v. 36, no. 5, p. 367-370, doi:
1098 10.1130/g24517a.1.
1099 Holdsworth, R. E., Handa, M., Miller, J. A., and Buick, I. S., 2001, Continental reactivation
1100 and reworking: an introduction: in Miller, J.A., Holdsworth, R.E., Buick, I.S., and
1101 Hand, M., eds., Continental Reactivation and Reworking: Geological Society, London,
1102 Special Publications, v. 184, no. 1, p. 1-12, doi: 10.1144/gsl.sp.2001.184.01.01.
1103 Hollingsworth, J., Fattahi, M., Walker, R., Talebian, M., Bahroudi, A., Bolourchi, M. J.,
1104 Jackson, J., and Copley, A., 2010, Oroclinal bending, distributed thrust and strike-slip
1105 faulting, and the accommodation of Arabia–Eurasia convergence in NE Iran since the
1106 Oligocene: Geophysical Journal International, v. 181, no. 3, p. 1214-1246, doi:
1107 10.1111/j.1365-246X.2010.04591.x.
1108 Homke, S., Vergés, J., Serra-Kiel, J., Bernaola, G., Sharp, I., Garcés, M., Montero-Verdú, I.,
1109 Karpuz, R., and Goodarzi, M. H., 2009, Late Cretaceous–Paleocene formation of the
1110 proto–Zagros foreland basin, Lurestan Province, SW Iran: Geological Society of
1111 America Bulletin, v. 121, no. 7-8, p. 963-978, doi: 10.1130/b26035.1.
1112 Homke, S., Vergés, J., Van Der Beek, P., Fernàndez, M., Saura, E., Barbero, L., Badics, B.,
1113 and Labrin, E., 2010, Insights in the exhumation history of the NW Zagros from
1114 bedrock and detrital apatite fission-track analysis: evidence for a long-lived orogeny:
1115 Basin Research, v. 22, no. 5, p. 659-680, doi: 10.1111/j.1365-2117.2009.00431.x.
1116 Hourigan, J.K., Reiners, P.W., Brandon, M.T., 2005. U-Th zonation-dependent alpha-
1117 ejection in (U-Th)/He chronometry. Geochimica et Cosmochimica Acta, Vol. 69, No.
1118 13, pp. 3349–3365, 2005

House, M.A., Farley, K.A., and Kohn, B.C., 1999, An empirical test of helium diffusion in apatite: borehole data from the Otway basin, Australia: Earth and Planetary Science Letters, v. 170, p. 463–474.

Jackson, J., and McKenzie, D., 1984, Active tectonics of the Alpine—Himalayan Belt between western Turkey and Pakistan: Geophysical Journal International, v. 77, no. 1, p. 185-264, doi: 10.1111/j.1365-246X.1984.tb01931.x.

Jackson, J., Priestley, K., Allen, M., and Berberian, M., 2002, Active tectonics of the South Caspian Basin: Geophysical Journal International, v. 148, no. 2, p. 214-245, doi: 10.1046/j.1365-246X.2002.01588.x.

Jalilian, M., Etemadi, N., Zadeh, A. A., Manouchehri, M., Pour, M. J. V., Tehrani, N. A., Behrouzi, A., Kholghi, M. H., and Naini, M. A., 1992, Geological Map of Torbat-e-Heydarieh: Geological Survey of Iran, scale 1:250000, Teheran, Iran.

Javadi, H. R., Ghassemi, M. R., Shahpasandzadeh, M., Guest, B., Ashtiani, M. E., Yassaghi, A., and Kouhpeyma, M., 2013, History of faulting on the Doruneh Fault System: implications for the kinematic changes of the Central Iranian Microplate: Geological Magazine, v. 150, no. 4, p. 651-672, doi: 10.1017/S0016756812000751.

Khadivi, S., Mouthereau, F., Barbarand, J., Adatte, T., and Lacombe, O., 2012, Constraints on palaeodrainage evolution induced by uplift and exhumation on the southern flank of the Zagros–Iranian Plateau: Journal of the Geological Society, v. 169, no. 1, p. 83-97, doi: 10.1144/0016-76492011-031.

Khadivi, S., Mouthereau, F., Larrasoaña, J. C., Vergés, J., Lacombe, O., Khademi, E., Beamud, E., Melinte-Dobrinescu, M., and Suc, J. P., 2010, Magnetochronology of synorogenic Miocene foreland sediments in the Fars arc of the Zagros Folded Belt (SW Iran): Basin Research, v. 22, no. 6, p. 918-932, doi: 10.1111/j.1365-2117.2009.00446.x.

1143 Le Guerroué, E., and Cobbold, P. R., 2006, Influence of erosion and sedimentation on strike-
1144 slip fault systems: insights from analogue models: Journal of Structural Geology, v. 28,
1145 no. 3, p. 421-430, doi: 10.1016/j.jsg.2005.11.007.
1146 Madanipour, S., Ehlers, T. A., Yassaghi, A., Rezaeian, M., Enkelmann, E., and Bahroudi, A.,
1147 2013, Synchronous deformation on orogenic plateau margins: Insights from the
1148 Arabia–Eurasia collision: Tectonophysics, v. 608, p. 440-451, doi:
1149 10.1016/j.tecto.2013.09.003.
1150 Matenco, L., Bertotti, G., Leever, K., Cloetingh, S., Schmid, S. M., Tărăpoancă, M., and
1151 Dinu, C., 2007, Large-scale deformation in a locked collisional boundary: Interplay
1152 between subsidence and uplift, intraplate stress, and inherited lithospheric structure in
1153 the late stage of the SE Carpathians evolution: Tectonics, v. 26, no. 4, doi:
1154 10.1029/2006tc001951.
1155 Mattei, M., Cifelli, F., Muttoni, G., Zanchi, A., Berra, F., Mossavvari, F., and Eshraghi, S. A.,
1156 2012, Neogene block rotation in central Iran: Evidence from paleomagnetic data:
1157 Geological Society of America Bulletin, v. 124, no. 5-6, p. 943-956, doi:
1158 10.1130/b30479.1.
1159 Meyer, B., and Le Dortz, K., 2007, Strike-slip kinematics in Central and Eastern Iran:
1160 Estimating fault slip-rates averaged over the Holocene: Tectonics, v. 26, no. 5, doi:
1161 10.1029/2006tc002073.
1162 Meyer, B., Mouthereau, F., Lacombe, O., and Agard, P., 2006, Evidence of Quaternary
1163 activity along the Deshir Fault: implication for the Tertiary tectonics of Central Iran:
1164 Geophysical Journal International, v. 164, no. 1, p. 192-201, doi: 10.1111/j.1365-
1165 246X.2005.02784.x.

1166 McClusky, S., Reilinger, R., Mahmoud, S., Ben Sari, D., and Tealeb, A., 2003, GPS
1167 constraints on Africa (Nubia) and Arabia plate motions: Geophysical Journal
1168 International, v. 155, no. 1, p. 126-138, doi: 10.1046/j.1365-246X.2003.02023.x.
1169 McQuarrie, N., and van Hinsbergen, D. J. J., 2013, Retrodeforming the Arabia-Eurasia
1170 collision zone: Age of collision versus magnitude of continental subduction: Geology,
1171 v. 41, no. 3, p. 315-318, doi: 10.1130/g33591.1.
1172 McQuarrie, N., Stock, J. M., Verdel, C., and Wernicke, B. P., 2003, Cenozoic evolution of
1173 Neotethys and implications for the causes of plate motions: Geophysical Research
1174 Letters, v. 30, no. 20, p. 2036, doi: 10.1029/2003gl017992.
1175 Molnar, P., 1988, Continental tectonics in the aftermath of plate tectonics: Nature, v. 335, no.
1176 6186, p. 131-137.
1177 Molnar, P., and Tapponnier, P., 1975, Cenozoic tectonics of Asia: effects of a continental
1178 collision: Science, v. 189, no. 4201, p. 419-426.
1179 Molnar, P., Anderson, R. S., and Anderson, S. P., 2007, Tectonics, fracturing of rock, and
1180 erosion: Journal of Geophysical Research: Earth Surface, v. 112, doi:
1181 10.1029/2005jf000433.
1182 Morley, C. K., Kongwung, B., Julapour, A. A., Abdolghafourian, M., Hajian, M., Waples, D.,
1183 Warren, J., Otterdoom, H., Srisuriyon, K., and Kazemi, H., 2009, Structural
1184 development of a major late Cenozoic basin and transpressional belt in central Iran: The
1185 Central Basin in the Qom-Saveh area: Geosphere, v. 5, no. 4, p. 325-362, doi:
1186 10.1130/ges00223.1.
1187 Morley, C. K., 2007, Variations in Late Cenozoic–Recent strike-slip and oblique-extensional
1188 geometries, within Indochina: The influence of pre-existing fabrics: Journal of
1189 Structural Geology, v. 29, no. 1, p. 36-58, doi: 10.1016/j.jsg.2006.07.003.

1190 Mouthereau, F., 2011, Timing of uplift in the Zagros belt/Iranian plateau and accommodation
1191 of late Cenozoic Arabia–Eurasia convergence: Geological Magazine, v. 148, no. 5-6, p.
1192 726-738, doi: doi:10.1017/S0016756811000306.
1193 Mouthereau, F., Tensi, J., Bellahsen, N., Lacombe, O., De Boisgrollier, T., and Kargar, S.,
1194 2007, Tertiary sequence of deformation in a thin-skinned/thick-skinned collision belt:
1195 The Zagros Folded Belt (Fars, Iran): Tectonics, v. 26, no. 5, doi: 10.1029/2007tc002098
1196 Mouthereau, F., Lacombe, O., and Vergés, J., 2012, Building the Zagros collisional orogen:
1197 Timing, strain distribution and the dynamics of Arabia/Eurasia plate convergence:
1198 Tectonophysics, v. 532–535, p. 27-60, doi: 10.1016/j.tecto.2012.01.022.
1199 Nozaem, R., Mohajjel, M., Rossetti, F., Della Seta, M., Vignaroli, G., Yassaghi, A., Salvini,
1200 F., and Eliassi, M., 2013, Post-Neogene right-lateral strike–slip tectonics at the north-
1201 western edge of the Lut Block (Kuh-e–Sarhangi Fault), Central Iran: Tectonophysics, v.
1202 589, p. 220-233, doi: 10.1016/j.tecto.2013.01.001.
1203 Okay, A. I., Zattin, M., and Cavazza, W., 2010, Apatite fission-track data for the Miocene
1204 Arabia-Eurasia collision: Geology, v. 38, no. 1, p. 35-38, doi: 10.1130/g30234.1.
1205 Paterson, M. S., and Wong, T.-F., 2005, Experimental rock deformation - The brittle field,
1206 Springer Science & Business Media, New York, 348 p.
1207 Pavlis, T. L., Enkelmann, E., Gulick, S. P. S., and Pavlis, G. L., 2014, Introduction: Neogene
1208 tectonics and climate-tectonic interactions in the southern Alaskan orogen themed
1209 issue: Geosphere, v. 10, no. 3, p. 424-427, doi: 10.1130/ges01023.1.
1210 Petit, J. P., 1987, Criteria for the sense of movement on fault surfaces in brittle rocks: Journal
1211 of Structural Geology, v. 9, no. 5–6, p. 597-608, doi: 10.1016/0191-8141(87)90145-3.
1212 Raimondo, T., Hand, M., and Collins, W. J., 2014, Compressional intracontinental orogens:
1213 Ancient and modern perspectives: Earth-Science Reviews, v. 130, p. 128-153, doi:
1214 10.1016/j.earscirev.2013.11.009.

1215 Ramezani, J., and Tucker, R. D., 2003, The Saghand Region, Central Iran: U-Pb
1216 geochronology, petrogenesis and implications for Gondwana Tectonics: American
1217 Journal of Science, v. 303, no. 7, p. 622-665, doi: 10.2475/ajs.303.7.622.
1218 Reading, H. G., 2009, Sedimentary environments: processes, facies and stratigraphy, John
1219 Wiley & Sons, Oxford, 704 p.
1220 Reece, R. S., Gulick, S. P. S., Christeson, G. L., Horton, B. K., van Avendonk, H., and Barth,
1221 G., 2013, The role of farfield tectonic stress in oceanic intraplate deformation, Gulf of
1222 Alaska: Journal of Geophysical Research: Solid Earth, v. 118, no. 5, p. 1862-1872, doi:
1223 10.1002/jgrb.50177.
1224 Regard, V., Bellier, O., Thomas, J.-C., Bourlès, D., Bonnet, S., Abbassi, M. R., Braucher, R.,
1225 Mercier, J., Shabanian, E., Soleymani, S., and Feghhi, K., 2005, Cumulative right-
1226 lateral fault slip rate across the Zagros—Makran transfer zone: role of the Minab—
1227 Zendan fault system in accommodating Arabia—Eurasia convergence in southeast Iran:
1228 Geophysical Journal International, v. 162, no. 1, p. 177-203, doi: 10.1111/j.1365-
1229 246X.2005.02558.x.
1230 Regard, V., Bellier, O., Braucher, R., Gasse, F., Bourlès, D., Mercier, J., Thomas, J. C.,
1231 Abbassi, M. R., Shabanian, E., and Soleymani, S., 2006, 10Be dating of alluvial
1232 deposits from Southeastern Iran (the Hormoz Strait area): Palaeogeography,
1233 Palaeoclimatology, Palaeoecology, v. 242, no. 1–2, p. 36-53, doi:
1234 10.1016/j.palaeo.2006.05.012.
1235 Regard, V., Hatzfeld, D., Molinaro, M., Aubourg, C., Bayer, R., Bellier, O., Yamini-Fard, F.,
1236 Peyret, M., and Abbassi, M., 2010, The transition between Makran subduction and the
1237 Zagros collision: recent advances in its structure and active deformation, in Leturmy,
1238 P., and Robin, C., eds., Tectonic and Stratigraphic Evolution of Zagros and Makran

during the Mesozoic–Cenozoic: Geological Society, London, Special Publications, v. 330, no. 1, p. 43-64, doi: 10.1144/sp330.4.

Reilinger, R., McClusky, S., Vernant, P., Lawrence, S., Ergintav, S., Cakmak, R., Ozener, H., Kadirov, F., Guliev, I., Stepanyan, R., Nadariya, M., Hahubia, G., Mahmoud, S., Sakr, K., ArRajehi, A., Paradissis, D., Al-Aydrus, A., Prilepin, M., Guseva, T., Evren, E., Dmitrotsa, A., Filikov, S. V., Gomez, F., Al-Ghazzi, R., and Karam, G., 2006, GPS constraints on continental deformation in the Africa-Arabia-Eurasia continental collision zone and implications for the dynamics of plate interactions: Journal of Geophysical Research: Solid Earth, v. 111, doi: 10.1029/2005jb004051.

Rezaeian, M., Carter, A., Hovius, N., and Allen, M. B., 2012, Cenozoic exhumation history of the Alborz Mountains, Iran: New constraints from low-temperature chronometry: Tectonics, v. 31, no. 2, doi: 10.1029/2011tc002974.

Robert, A. M. M., Letouzey, J., Kavoosi, M. A., Sherkati, S., Müller, C., Vergés, J., and Aghababaei, A., 2014, Structural evolution of the Kopeh Dagh fold-and-thrust belt (NE Iran) and interactions with the South Caspian Sea Basin and Amu Darya Basin: Marine and Petroleum Geology, v. 57, p. 68-87, doi: 10.1016/j.marpetgeo.2014.05.002.

Robertson, A. H. F., Ustaömer, T., Parlak, O., Ünlügenç, U. C., Taşlı, K., and İnan, N., 2006, The Berit transect of the Tauride thrust belt, S Turkey: Late Cretaceous–Early Cenozoic accretionary/collisional processes related to closure of the Southern Neotethys: Journal of Asian Earth Sciences, v. 27, no. 1, p. 108-145, doi: 10.1016/j.jseaes.2005.02.004.

Ron, H., Freund, R., Garfunkel, Z., and Nur, A., 1984, Block rotation by strike-slip faulting: Structural and paleomagnetic evidence: Journal of Geophysical Research: Solid Earth, v. 89, p. 6256-6270, doi: 10.1029/JB089iB07p06256.

Rossetti, F., Lisker, F., Storti, F., and Läufer, A. L., 2003, Tectonic and denudational history of the Rennick Graben (North Victoria Land): Implications for the evolution of rifting

between East and West Antarctica: Tectonics, v. 22, no. 2, p. 1016, doi: 10.1029/2002tc001416.

Rossetti, F., Nozaem, R., Lucci, F., Vignaroli, G., Gerdes, A., Nasrabadi, M., and Theye, T., 2015, Tectonic setting and geochronology of the Cadomian (Ediacaran-Cambrian) magmatism in Central Iran, Kuh-e-Sarhangi region (NW Lut Block): Journal of Asian Earth Sciences, v. 102, p. 24-44, doi: 10.1016/j.jseaes.2014.07.034.

Rowland, J. V., and Sibson, R. H., 2004, Structural controls on hydrothermal flow in a segmented rift system, Taupo Volcanic Zone, New Zealand: Geofluids, v. 4, no. 4, p. 259-283, doi: 10.1111/j.1468-8123.2004.00091.x.

Rutter, E. H., and Hadizadeh, J., 1991, On the influence of porosity on the low-temperature brittle—ductile transition in siliciclastic rocks: Journal of Structural Geology, v. 13, no. 5, p. 609-614, doi: 10.1016/0191-8141(91)90047-M.

Salvini, F., 2004, Daisy 3 The Structural Data Integrated System Analyzer., p. Available at Software University of Roma Tre, Roma: http://host.uniroma3.it/progetti/fralab.

Salvini, F., Brancolini, G., Busetti, M., Storti, F., Mazzarini, F., and Coren, F., 1997, Cenozoic geodynamics of the Ross Sea region, Antarctica: Crustal extension, intraplate strike-slip faulting, and tectonic inheritance: Journal of Geophysical Research: Solid Earth, v. 102, p. 24669-24696, doi: 10.1029/97jb01643.

Sanderson, D. J., and Marchini, W. R. D., 1984, Transpression: Journal of Structural Geology, v. 6, no. 5, p. 449-458, doi: 10.1016/0191-8141(84)90058-0.

Sandiford, M., Wallace, M., and Coblentz, D., 2004, Origin of the in situ stress field in south-eastern Australia: Basin Research, v. 16, no. 3, p. 325-338, doi: 10.1111/j.1365-2117.2004.00235.x.

Scholz, C. H., 2002, The mechanics of earthquakes and faulting, Cambridge university press.

1288 Schopfer, M. P., and Steyrer, H. P., 2001, Experimental modeling of strike-slip faults and the
1289 self-similar behavior: Memoirs of the Geological Society of America, p. 21-28.

1290 Schrank, C. E., and Cruden, A. R., 2010, Compaction control of topography and fault
1291 network structure along strike-slip faults in sedimentary basins: Journal of Structural
1292 Geology, v. 32, no. 2, p. 184-191, doi: 10.1016/j.jsg.2009.11.003.
1293 Sella, G. F., Dixon, T. H., and Mao, A., 2002, Revel: A model for recent plate velocities from
1294 space geodesy: Journal of Geophysical Research, v. 107, no. 10.1029, p. 209-226,
1295 doi:10.1029/2000JB000033.

1296 Shabanian, E., Bellier, O., Siame, L., Arnaud, N., Abbassi, M. R., and Cochemé, J.-J., 2009a,
1297 New tectonic configuration in NE Iran: Active strike-slip faulting between the Kopeh
1298 Dagh and Binalud mountains: Tectonics, v. 28, no. 5, doi: 10.1029/2008tc002444.
1299 Shabanian, E., Siame, L., Bellier, O., Benedetti, L., and Abbassi, M. R., 2009b, Quaternary
1300 slip rates along the northeastern boundary of the Arabia-Eurasia collision zone (Kopeh
1301 Dagh Mountains, Northeast Iran): Geophysical Journal International, v. 178, no. 2, p.
1302 1055-1077, doi: 10.1111/j.1365
1303 Shabanian, E., Bellier, O., Abbassi, M. R., Siame, L., and Farbod, Y., 2010, Plio-Quaternary
1304 stress states in NE Iran: Kopeh Dagh and Allah Dagh-Binalud mountain ranges:
1305 Tectonophysics, v. 480, no. 1–4, p. 280-304, doi: 10.1016/j.tecto.2009.10.022.-
1306 246X.2009.04183.x.
1307 Sheldon, H. A., Barnicoat, A. C., and Ord, A., 2006, Numerical modelling of faulting and
1308 fluid flow in porous rocks: An approach based on critical state soil mechanics: Journal
1309 of Structural Geology, v. 28, no. 8, p. 1468-1482, doi: 10.1016/j.jsg.2006.03.039.
1310 Simons, W. J. F., Socquet, A., Vigny, C., Ambrosius, B. A. C., Haji Abu, S., Promthong, C.,
1311 Subarya, C., Sarsito, D. A., Matheussen, S., Morgan, P., and Spakman, W., 2007, A

1312 decade of GPS in Southeast Asia: Resolving Sundaland motion and boundaries: Journal
1313 of Geophysical Research: Solid Earth, v. 112, doi: 10.1029/2005jb003868.
1314 Spotila, J. A., Farley, K. A., and Sieh, K., 1998, Uplift and erosion of the San Bernardino
1315 Mountains associated with transpression along the San Andreas fault, California, as
1316 constrained by radiogenic helium thermochronometry: Tectonics, v. 17, no. 3, doi:
1317 10.1029/98tc00378.
1318 Spotila, J. A., Farley, K. A., Yule, J. D., and Reiners, P. W., 2001, Near-field transpressive
1319 deformation along the San Andreas fault zone in southern California, based on
1320 exhumation constrained by (U-Th)/He dating: Journal of Geophysical Research: Solid
1321 Earth, v. 106, p. 30909-30922, doi: 10.1029/2001jb000348.
1322 Spotila, J. A., Niemi, N., Brady, R., House, M., Buscher, J., and Oskin, M., 2007b, Long-
1323 term continental deformation associated with transpressive plate motion: The San
1324 Andreas fault: Geology, v. 35, no. 11, p. 967-970, doi: 10.1130/g23816a.1.
1325 Storti, F., Holdsworth, R. E., and Salvini, F., 2003, Intraplate strike-slip deformation belts:
1326 Geological Society, London, Special Publications, v. 210, no. 1, p. 1-14, doi:
1327 10.1144/gsl.sp.2003.210.01.01.
1328 Sutton, J., and Watson, J. V., 1986, Architecture of the Continental Lithosphere:
1329 Philosophical Transactions of the Royal Society of London A: Mathematical, Physical
1330 and Engineering Sciences, v. 317, no. 1539, p. 5-12.
1331 Sylvester, A. G., 1988, Strike-slip faults: Geological Society of America Bulletin, v. 100, no.
1332 11, p. 1666-1703, doi: 10.1130/0016-7606(1988)100<1666:ssf>2.3.co;2.
1333 Tapponier, P., and Molnar, P., 1977, Active faulting and tectonics in China: Journal of
1334 Geophysical Research, v. 82, p. 2905-2930, doi: 10.1029/JB082i020p02905.
1335 Tavarnelli, E., 1998, Tectonic evolution of the Northern Salinian Block, California, USA:
1336 Paleogene to Recent shortening in a transform fault-bounded continetal fragment, *in*:

1337 Holdworth, R.E., Strachan, R.A., Dewey, J.E., eds. 1998. Continental Transpressional
1338 and Transtensional Tectonics, Geological Society, London, Special Publications 135, p.
1339 107-118.
1340 Tavarnelli, E., and Holdsworth, R. E., 1999, How long do structures take to form in
1341 transpression zones? A cautionary tale from California: Geology, v. 27, no. 12, p. 1063-
1342 1066, doi: 10.1130/0091-7613(1999)027<1063:hldstt>2.3.co;2.
1343 Tavarnelli, E., and Pasqui, V, 2000, Fault growth by segment linkage in seismically active
1344 settings: Examples from the Southern Apennines, Italy, and the Coast Ranges,
1345 California: Journal of Geodynamics, v. 29, p. 501-516.
1346 Tchalenko, J. S., Berberian, M., and Behzadi, H., 1973, Geomorph1c and seismic evidence
1347 for recent activity on the Doruneh Fault, Iran: Tectonophysics, v. 19, no. 4, p. 333-341,
1348 doi: 10.1016/0040-1951(73)90027-9.
1349 Verdel, C., Wernicke, B. P., Ramezani, J., Hassanzadeh, J., Renne, P. R., and Spell, T. L.,
1350 2007, Geology and thermochronology of Tertiary Cordilleran-style metamorphic core
1351 complexes in the Saghand region of central Iran: Geological Society of America
1352 Bulletin, v. 119, no. 7-8, p. 961-977, doi: 10.1130/b26102.1.
1353 Vernant, P., Nilforoushan, F., Hatzfeld, D., Abbassi, M. R., Vigny, C., Masson, F., Nankali,
1354 H., Martinod, J., Ashtiani, A., Bayer, R., Tavakoli, F., and Chéry, J., 2004, Present-day
1355 crustal deformation and plate kinematics in the Middle East constrained by GPS
1356 measurements in Iran and northern Oman: Geophysical Journal International, v. 157,
1357 no. 1, p. 381-398, doi: 10.1111/j.1365-246X.2004.02222.x.
1358 Vincent, S. J., Morton, A. C., Carter, A., Gibbs, S., and Barabadze, T. G., 2007, Oligocene
1359 uplift of the Western Greater Caucasus: an effect of initial Arabia–Eurasia collision:
1360 Terra Nova, v. 19, no. 2, p. 160-166, doi: 10.1111/j.1365-3121.2007.00731.x.

1361 Walker, R., and Jackson, J., 2004, Active tectonics and late Cenozoic strain distribution in
1362 central and eastern Iran: Tectonics, v. 23, no. 5, doi: 10.1029/2003tc001529.
1363 Walker, R., Jackson, J., and Baker, C., 2004, Active faulting and seismicity of the Dasht-e-
1364 Bayaz region, eastern Iran: Geophysical Journal International, v. 157, no. 1, p. 265-282,
1365 doi: 10.1111/j.1365-2966.2004.02179.x.
1366 Walker, R. T., and Fattahi, M., 2011, A framework of Holocene and Late Pleistocene
1367 environmental change in eastern Iran inferred from the dating of periods of alluvial fan
1368 abandonment, river terracing, and lake deposition: Quaternary Science Reviews, v. 30,
1369 no. 9–10, p. 1256-1271, doi: 10.1016/j.quascirev.2011.03.004.
1370 Walker, R. T., and Khatib, M. M., 2006, Active faulting in the Birjand region of NE Iran:
1371 Tectonics, v. 25, no. 4, doi: 10.1029/2005tc001871.
1372 Walpersdorf, A., Manighetti, I., Mousavi, Z., Tavakoli, F., Vergnolle, M., Jadidi, A.,
1373 Hatzfeld, D., Aghamohammadi, A., Bigot, A., Djamour, Y., Nankali, H., and Sedighi,
1374 M., 2014, Present-day kinematics and fault slip rates in eastern Iran, derived from 11
1375 years of GPS data: Journal of Geophysical Research: Solid Earth, v. 119, no. 2, doi:
1376 10.1002/2013jb010620.
1377 Webb, L. E., and Johnson, C. L., 2006, Tertiary strike-slip faulting in southeastern Mongolia
1378 and implications for Asian tectonics: Earth and Planetary Science Letters, v. 241, no. 1–
1379 2, p. 323-335, doi: 10.1016/j.epsl.2005.10.033.
1380 Wong, T.-f., and Baud, P., 2012, The brittle-ductile transition in porous rock: A review:
1381 Journal of Structural Geology, v. 44, no. 0, p. 25-53, doi: 10.1016/j.jsg.2012.07.010.
1382 Woodcock, N., and Schubert, C., 1994, Continental strike-slip tectonics: Continental
1383 deformation, in Hancock, P.L., ed., Continental Deformation: Pergamon Press, Oxford,
1384 p. 251-263.

1385 Woodcock, N. H., and Fischer, M., 1986, Strike-slip duplexes: Journal of Structural Geology,
1386 v. 8, no. 7, p. 725-735, doi: 10.1016/0191-8141(86)90021-0.
1387 Woodcock, N. H., and Rickards, B., 2003, Transpressive duplex and flower structure: Dent
1388 Fault System, NW England: Journal of Structural Geology, v. 25, no. 12, p. 1981-1992.
1389 Wu, J. E., McClay, K., Whitehouse, P., and Dooley, T., 2009, 4D analogue modelling of
1390 transtensional pull-apart basins: Marine and Petroleum Geology, v. 26, no. 8, p. 1608-
1391 1623, doi: 10.1016/j.marpetgeo.2008.06.007
1392 Ziegler, P. A., van Wees, J.-D., and Cloetingh, S., 1998, Mechanical controls on collision-
1393 related compressional intraplate deformation: Tectonophysics, v. 300, no. 1–4, p. 103-
1394 129, doi: 10.1016/S0040-1951(98)00236-4.
1395 Zoback, M. L., 1992, First- and second-order patterns of stress in the lithosphere: The World
1396 Stress Map Project: Journal of Geophysical Research: Solid Earth, v. 97, p. 11703-
1397 11728, doi: 10.1029/92jb00132.

1398

1399 **FIGURE CAPTIONS**

1400 Figure 1. Simplified tectonic map of Iran, showing the main collisional and intraplate strike–
1401 slip fault domains accommodating the Arabia-Eurasia convergence (modified after Berberian
1402 and King, 1981). The dashed rectangle indicates the study area. AF: Anar Fault; DBF: Dasht-
1403 e–Bayaz Fault; DF: Doruneh Fault; DSF: Dehshir fault; KKF Kalmard-Kuhbanan Fault,
1404 KKTZ, Kashmar-Kerman Tectonic Zone, KSF: Kuh-e–Sarhangi Fault; MZT: Main Zagros
1405 Trust; NBF: Nayband Fault; NHF: Nehbandan fault; SBF: Shahr-e–Babak Fault; ZMTZ:
1406 Zagros-Makran Transfer Zone. The GPS velocities vectors in Iran relative to stable Eurasia
1407 are shown with different colors after Vernant et al. (2004) and Walpersdorf et al. (2014).

1408

1409 Figure 2. Simplified tectonic map of northern central Iran, showing the historical and
1410 instrumental seismicity of the area. Focal mechanisms are taken from the Harvard catalog
1411 (http://www.globalcmt.org/CMTsearch.html). Epicenters are from the International Seismic
1412 Centre EHB Bulletin (International Seismic Centre, Thatcham, UK, 2009,
1413 (http://www.isc.ac.uk) and earthquake catalogue at Iranian Institute of Earthquake
1414 Engineering and Seismology (http://www.iiees.ac.ir). The dashed rectangle indicates the
1415 location of the study area and the extent of the map in Figure 3. DF—Doruneh fault; KSF—
1416 Kuh-e-Sarhangi fault; KFF—Kuh-e-Faghan fault; JTF—Jangal Thrust Fault; DBF— Dasht-
1417 e-Bayaz fault.

1418

1419 Figure 3. Structural map of the study area and interpretative geological cross-section (solid
1420 lines) across the structure of the Kuh-e-Faghan Fault. The inset shows the cumulative
1421 structural data set showing the bedding attitude (projected as pole to plane on a Schmidt net,
1422 lower emisphere projection), in the Neogene deposits and the Cumulative polymodal

1423 Gaussian statistics (with errors quoted at 1σ (sd) level) as obtained from the collected fault
1424 population. Results are shown as rose diagram for strikes, and frequency distribution
1425 histograms for dip and slickenline pitch values (Data processing through the software
1426 DAISY3 (Salvini, 2004; http://host.uniroma3.it/progetti/fralab/).
1427
1428 Figure 4. (A) Panoramic view showing the three Neogene sedimentary cycles and their
1429 stratigraphic relations. Contacts between Cycle-1 and Cycle deposits are bounded by a
1430 steeply-dipping fault zone. View locking northward; length of the stratigraphic section about
1431 4 km. (B) Panoramic view of Cycle-1 deposits onlapping onto the Paleozoic and Mesozoic
1432 basement. Note the angular contact between the basal breccias (Ng-B) and the upper Ng-C
1433 fluvial conglomerates. The inserts show the characteristic sedimentary structures of the
1434 deposits. Cycle-3 onlaps directly onto Cycle-1. (C) Progressive angular unconformities
1435 within Cycle-2. The inserts show the range of sedimentary structure observed within Cycle-2
1436 attesting for its fluvio-palustrine depositional environment. (d) panoramic view showing
1437 Cycle-3 onlapping directly onto the Paleozoic and Mesozoic basements units. Bedding strike
1438 and dip measurement are marked by white dots. The inserts show the range of sedimentary
1439 structure observed within the basal unit of Cycle-3 attesting for its lacustrine/playa lake
1440 depositional environment. The white dotted line shows the contact between Neogene
1441 sediments and basement units. In all figures, the white dots indicate points of bedding attitude
1442 measurements (in degrees, right-hand rule)
1443
1444 Figure 5. Generalized vertical stratigraphic section (GVS) of the Neogene deposits for the
1445 northern (A) and southern (B) sector of the study area. The series of stick-logs report the unit
1446 thicknesses measured along the relative geological transects (AB, CD, EF, EF2, GH, IJ, KL)
1447 shown in Fig. 3. Scale and legend in (A) apply to both figures.

Figure 6. Structures along the WFS. (A) Panoramic view (looking eastward), showing the core of the antiformal structure defined by the structural arrangement of the Cycle-1 Neogene conglomerates (Ng-C) (field of view 500 m). Note steepening of the southward limb approaching the WFS trace (red arrows). The fault zone is defined by verticalized panels of cataclastic conglomerates (Ng-C) in tectonic contact with the Cycle-3 gypsiferous marls (Ng-GM). The stereoplot (Schmidt net, lower hemisphere projection) details the collected fault data set (the longer arrow indicates the hanging wall direction of slip and its length relates to the horizontal component of slip; double half arrow indicates the sense of the strike-slip component). (B) The eastward termination of the WFS. Panoramic view (looking westward), showing the sub-vertical , ~400 meter thick damage zone associated with the NE bending of the WFS, which abruptly interrupts the monoclinal attitude of the Ng-C deposits. The fault zone involves the Quaternary alluvial and terraced deposits. (C) Hectometer-scale drag folding affecting the Neogene deposits when approaching the trace of the WFS and interpretative line drawing (see Fig. 3 for lithological symbols). The anticline is E/SE-plunging with an axial trace at an angle to the fault trace. Stereoplot (Schmidt net, lower hemisphere projection) showing the collected fault data. Fault slip is dominated by dextral and reverse kinematics along NE-SW striking steeply-dipping fault strands. See Figure 3 for location of the field pictures.

Figure 7. Structures along the WFS. (A) The basement-Neogene fault contact along the western tip of the CFS (looking westward) and interpretative line drawing (see Fig. 3 for lithological symbols), showing the fault zone architecture and fault zone localization along the verticalized weaker basement shale units. The stereoplot details the collected fault data set (Schmidt net, lower hemisphere projection). (B) Mesoscale NW-SE striking fault systems in

1473 the Ng-GM deposits along the eastward termination of the WFS. Note the syn-sedimentary
1474 character of faulting: the faults (red arrow) die out upwards into the sediments (yellow
1475 arrow). The stereoplot (Schmidt net, lower hemisphere projection) details the collected fault
1476 data set (the longer arrow indicates the hanging wall direction of slip and its length relates to
1477 the horizontal component of slip; double half arrow indicates the sense of the strike-slip
1478 component). WNW-ESE dextral and oblique (transtensional)- and normal-slip faults are
1479 observed. See Figure 3 for location of field pictures.
1480
1481 Figure 8. (A) Panoramic view (looking northeastward) of the prominent break in slope that
1482 defines the trace of the EFS, bounding Neogene (Ng-C) and Quaternary deposits. (B)
1483 Structural architecture of the fault zone across the EFS, exhibiting pluridecameter-thick, sub-
1484 vertical damage zone and fault core. The stereoplot (Schmidt net, lower hemisphere
1485 projection) shows the collected fault data set (the longer arrow indicates the hanging wall
1486 direction of slip and its length relates to the horizontal component of slip; double half arrow
1487 indicates the sense of the strike-slip component). Faulting is dominated by WNW-ESE
1488 striking dextral faults associated to minor antithetic NNE-SSW striking sinistral ones. (C)-(D)
1489 Examples of polished, E-W striking, hematite-coated fault surfaces, exhibiting prominent
1490 sub-horizontal striations. The kinematic indicators as provided by synthetic Riedel shears,
1491 lunate fractures and abrasion steps attest for dextral kinematics. See Figure 3 for location of
1492 field pictures.
1493
1494 Figure 9. (A) Outcrop-scale and schematic line drawing (B) showing S-C tectonites
1495 developed along the main trace of the EFS bounding the basement-Neogene (Ng-C) contact
1496 (See Figure 3 for location of field picture). Note the occurrence of meter-thick, E-W striking
1497 sub-vertical ultracataclastic dextral slip zones that bound the main fault rock types. (C)

Stereoplot (Schmidt net, lower hemisphere projection) showing the angular relationships between the S-C fabrics, the vein array and the main strike-slip fault surfaces. In the stereoplot, the longer arrow indicates the hanging wall direction of slip and its length relates to the horizontal component of slip. Double half arrow indicates the sense of the strike-slip component.

Figure 10. Quaternary faults. (A) Outcrop picture and line drawing (B) showing fault strands cutting though the Neogene (Ng-C) and the overlying Quaternary alluvial deposits shown in Fig. 6B. (C) Stereoplot showing the collected fault data (Schmidt net, lower hemisphere projection) set in the locality of Fig. 10A. The faults strike NE-SW and show dextral and reverse kinematics. Steeply-dipping NE-SW dextral and reverse faults cutting through and involving Neogene and Quaternary deposits. (D) E-W striking dextral fault cutting trough alluvial Quaternary deposits overlying Cycle-3 Ng-GM deposits. (E) Stereoplot showing the collected fault data set (Schmidt net, lower hemisphere projection) in the locality of Fig. 10D. In the stereonet, the longer arrow indicates the hanging wall direction of slip and its length relates to the horizontal component of slip. Double half arrows indicates the sense of the strike-slip component. See Figure 3 for location of field picutures.

Figure 11. (A) Structural map of the Kuh-e-Faghan Fault on shaded Topographic Elevation Model, showing the locations of the samples used for AHe thermochronometry, together with mean age results from each sample indicated (see Table 1). (B) Distribution of AHe sample elevations and ages projected to an alongs-strike topographic SWATH profile (40 times vertical exaggeration) along the KFF.

Figure 12. Conceptual spatio-temporal model for the long-term evolution of the Kuh-e-Faghan dextral fault system (see text for further details). Key to the figure: dark grey areas with plus (+); uplift; light grey areas with minus (-), subsidence; red, active fault; orange inactive fault. The black dot indicates the hypothetical exhumation path followed by the basement rocks during the punctuated tectonic activity of the KFF. For lithological symbols refer to Fig. 3.

TABLE 1 - Apatite (U+Th)/He Data

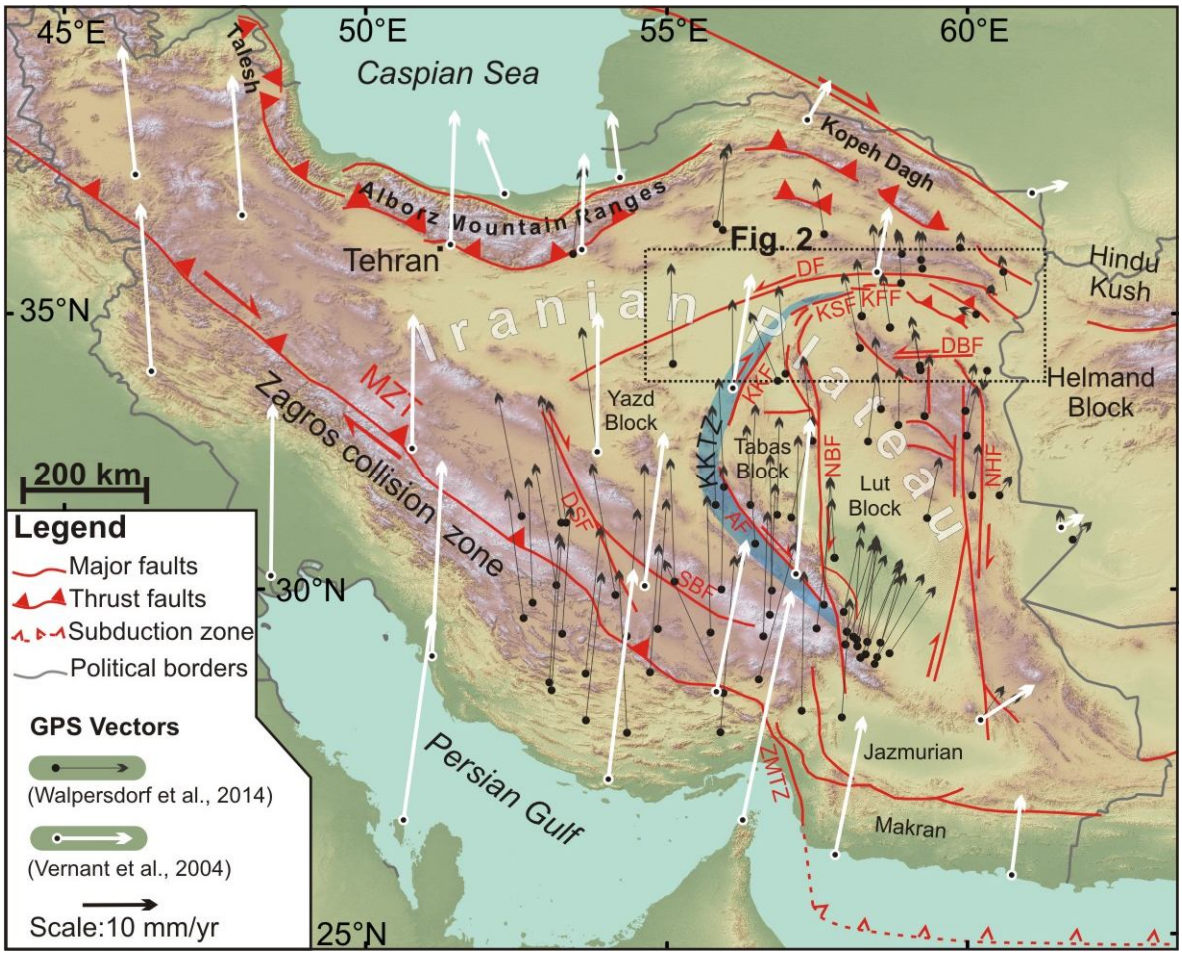

1534

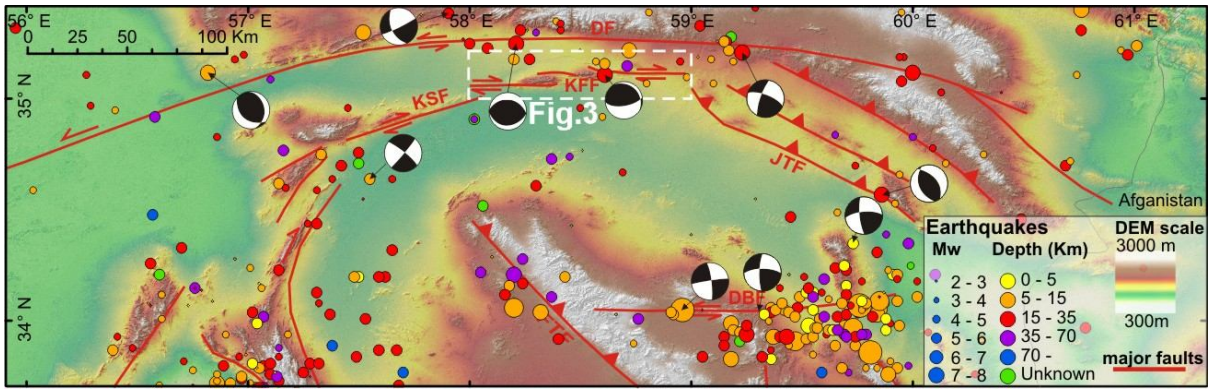

1535

1536

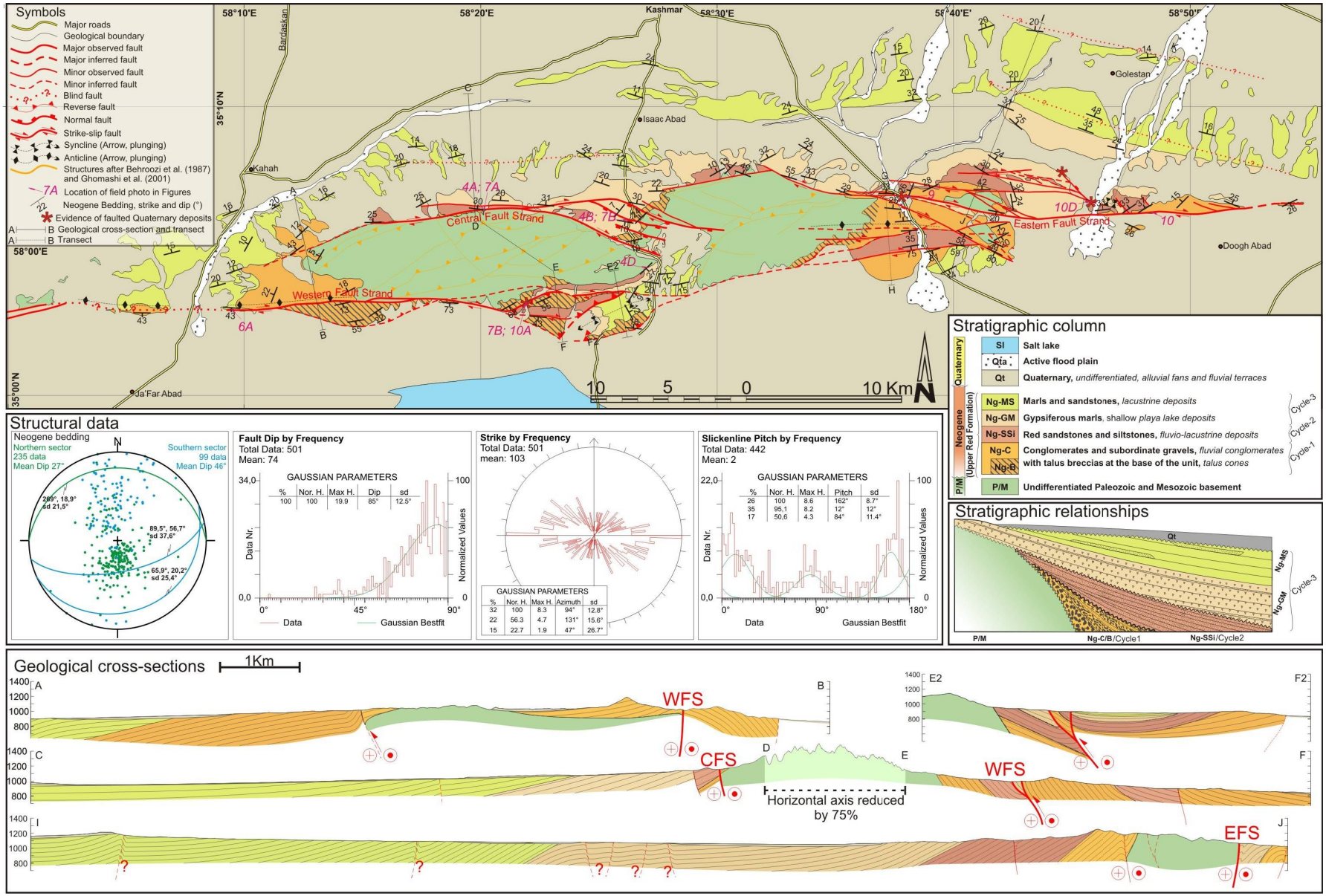
Symbols
Major roads
Geological boundary
Major observed fault
Major inferred fault
Minor observed fault
Minor inferred fault
Blind fault
Reverse fault
Normal fault
Strike-slip fault
Syncline (Arrow, plunging)
Anticline (Arrow, plunging)
Structures after Behroozi et al. (1987) and Ghomashi et al. (2001)
7A Location of field photo in Figures
Neogene Bedding, strike and dip (°)
Evidence of faulted Quaternary deposits
A B Geological cross-section and transect
A B Transect
58°10'E
58°20'E
58°30'E
58°40'E
58°50'E
35°10'N
35°00'N
58°00'E
Bardaskan
Kashmar
Golestan
Isaac Abad
Kahah
Doogh Abad
Ja'Far Abad
Central Fault Strand
Western Fault Strand
Eastern Fault Strand
4A; 7A
4B; 7B
4D
6A
7B; 10A
10D
10
10 5 0 10 Km
Structural data
Neogene bedding
Northern sector
235 data
Mean Dip 27°
Southern sector
99 data
Mean Dip 46°
269°, 18,9°
sd 21,5°
89,5°, 56,7°
sd 37,6°
65,9°, 20,2°
sd 25,4°
Fault Dip by Frequency
Total Data: 501
Mean: 74
GAUSSIAN PARAMETERS
% Nor. H. Max H. Dip sd
100 100 19.9 85° 12.5°
Data Nr.
Normalized Values
Data
Gaussian Bestfit
Strike by Frequency
Total Data: 501
mean: 103
GAUSSIAN PARAMETERS
% Nor. H. Max H. Azimuth sd
32 100 8.3 94° 12.8°
22 56.3 4.7 131° 15.6°
15 22.7 1.9 47° 26.7°
Slickenline Pitch by Frequency
Total Data: 442
Mean: 2
GAUSSIAN PARAMETERS
% Nor. H. Max H. Pitch sd
26 100 8.6 162° 8.7°
35 95,1 8.2 12° 12°
17 50,6 4.3 84° 11.4°
Stratigraphic column
Quaternary
Neogene (Upper Red Formation)
P/M
SI Salt lake
Qfa Active flood plain
Qt Quaternary, undifferentiated, alluvial fans and fluvial terraces
Ng-MS Marls and sandstones, lacustrine deposits
Ng-GM Gypsiferous marls, shallow playa lake deposits
Ng-SSi Red sandstones and siltstones, fluvio-lacustrine deposits
Ng-C Conglomerates and subordinate gravels, fluvial conglomerates
Ng-B with talus breccias at the base of the unit, talus cones
P/M Undifferentiated Paleozoic and Mesozoic basement
Cycle-3
Cycle-2
Cycle-1
Stratigraphic relationships
Qt
Ng-MS
Ng-GM
Cycle-3
P/M
Ng-C/B/Cycle1
Ng-SSi/Cycle2
Geological cross-sections
1Km
WFS
CFS
EFS
Horizontal axis reduced by 75%

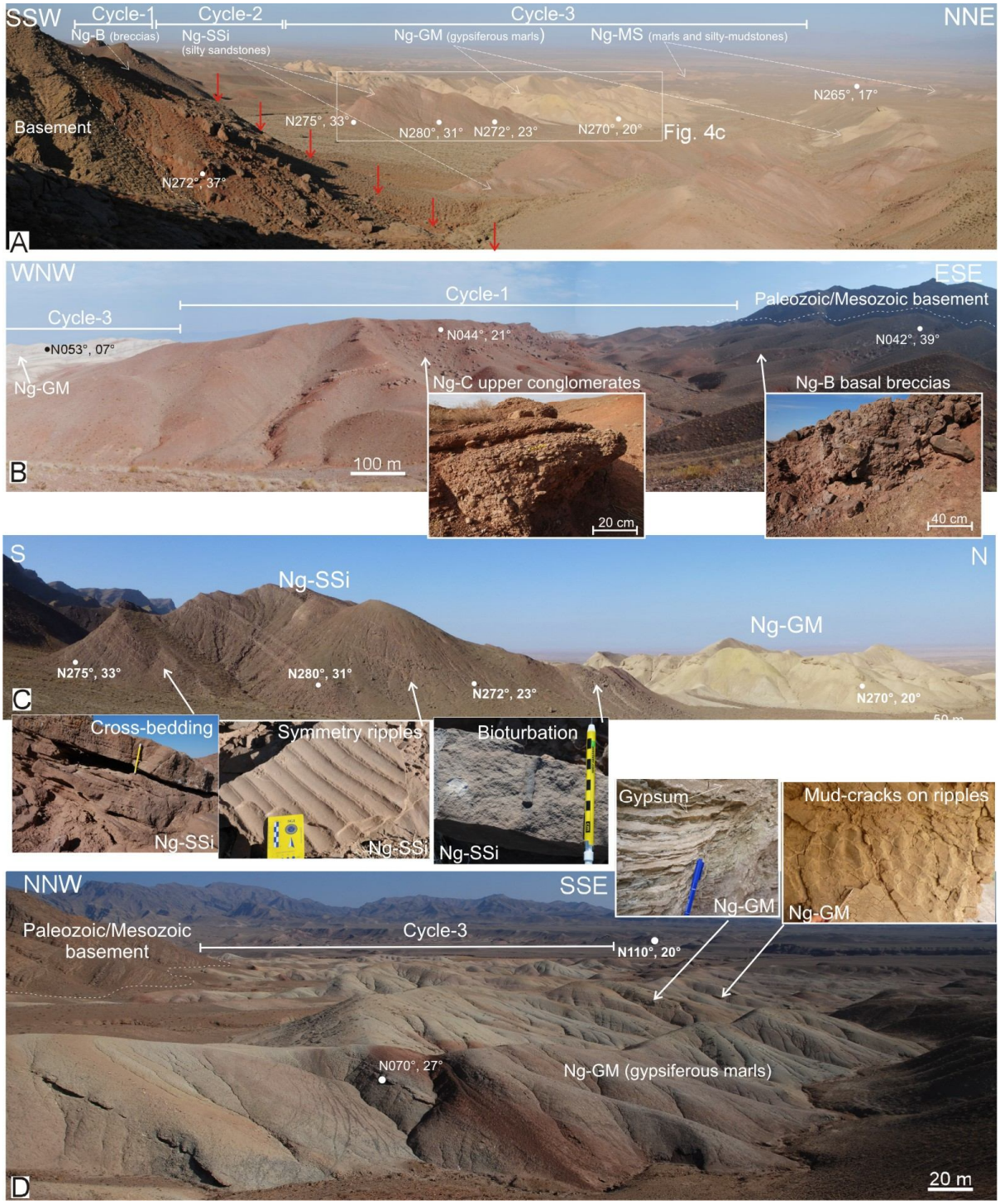
SSW
Cycle-1
Ng-B (breccias)
Cycle-2
Ng-SSi
(silty sandstones)
Cycle-3
Ng-GM (gypsiferous marls)
Ng-MS (marls and silty-mudstones)
NNE
Basement
N275°, 33°
N280°, 31°
N272°, 23°
N270°, 20°
N265°, 17°
N272°, 37°
Fig. 4c
A
WNW
Cycle-3
Cycle-1
ESE
Paleozoic/Mesozoic basement
N053°, 07°
Ng-GM
N044°, 21°
N042°, 39°
Ng-C upper conglomerates
Ng-B basal breccias
100 m
20 cm
40 cm
B
S
N
Ng-SSi
Ng-GM
N275°, 33°
N280°, 31°
N272°, 23°
N270°, 20°
C
Cross-bedding
Ng-SSi
Symmetry ripples
Ng-SSi
Bioturbation
Ng-SSi
Gypsum
Ng-GM
Mud-cracks on ripples
Ng-GM
NNW
SSE
Paleozoic/Mesozoic basement
Cycle-3
N110°, 20°
N070°, 27°
Ng-GM (gypsiferous marls)
20 m
D

1538

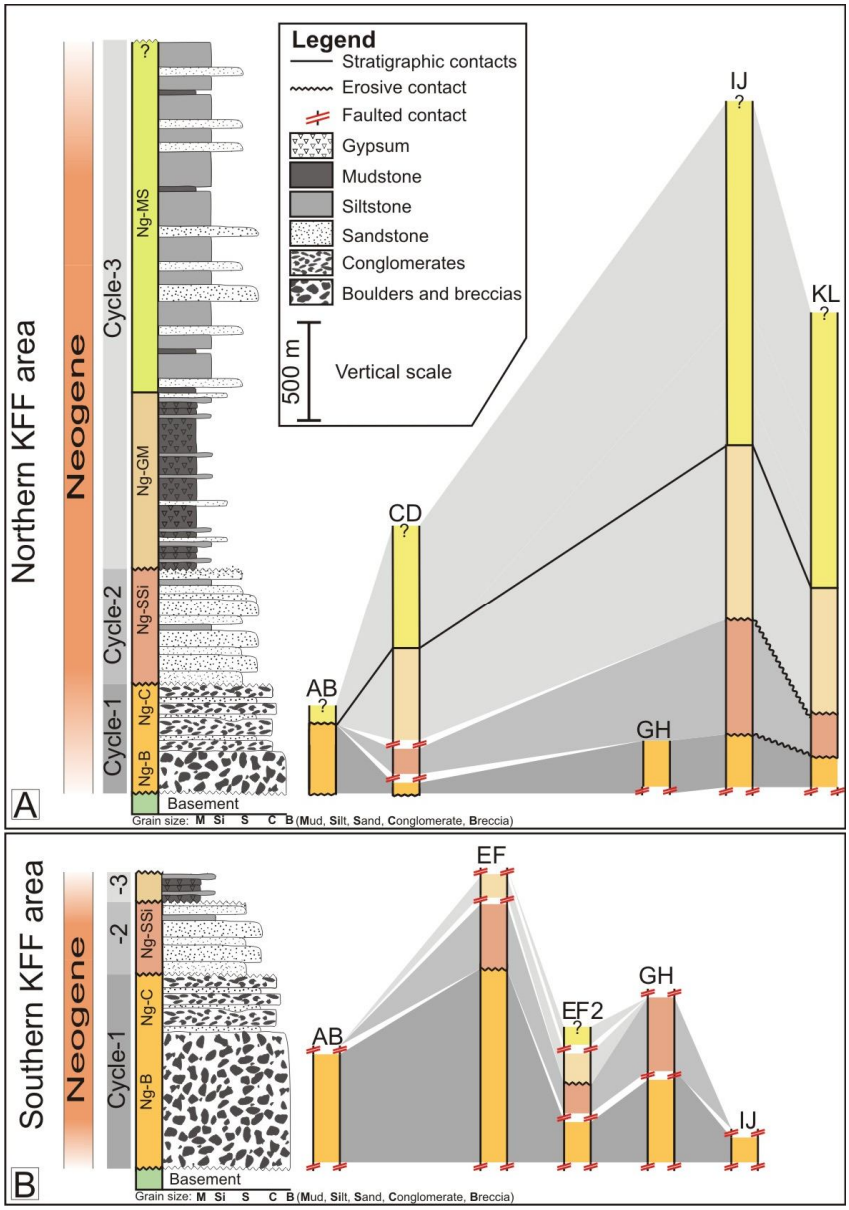
Northern KFF area
Neogene
Cycle-3
Cycle-2
Cycle-1
Ng-MS
Ng-GM
Ng-SSi
Ng-C
Ng-B
Basement
Legend
Stratigraphic contacts
Erosive contact
Faulted contact
Gypsum
Mudstone
Siltstone
Sandstone
Conglomerates
Boulders and breccias
500 m
Vertical scale
AB
CD
GH
IJ
KL
A
Grain size: M Si S C B (Mud, Silt, Sand, Conglomerate, Breccia)
Southern KFF area
Neogene
-3
-2
Cycle-1
Ng-SSi
Ng-C
Ng-B
Basement
AB
EF
EF2
GH
IJ
B
Grain size: M Si S C B (Mud, Silt, Sand, Conglomerate, Breccia)

1539

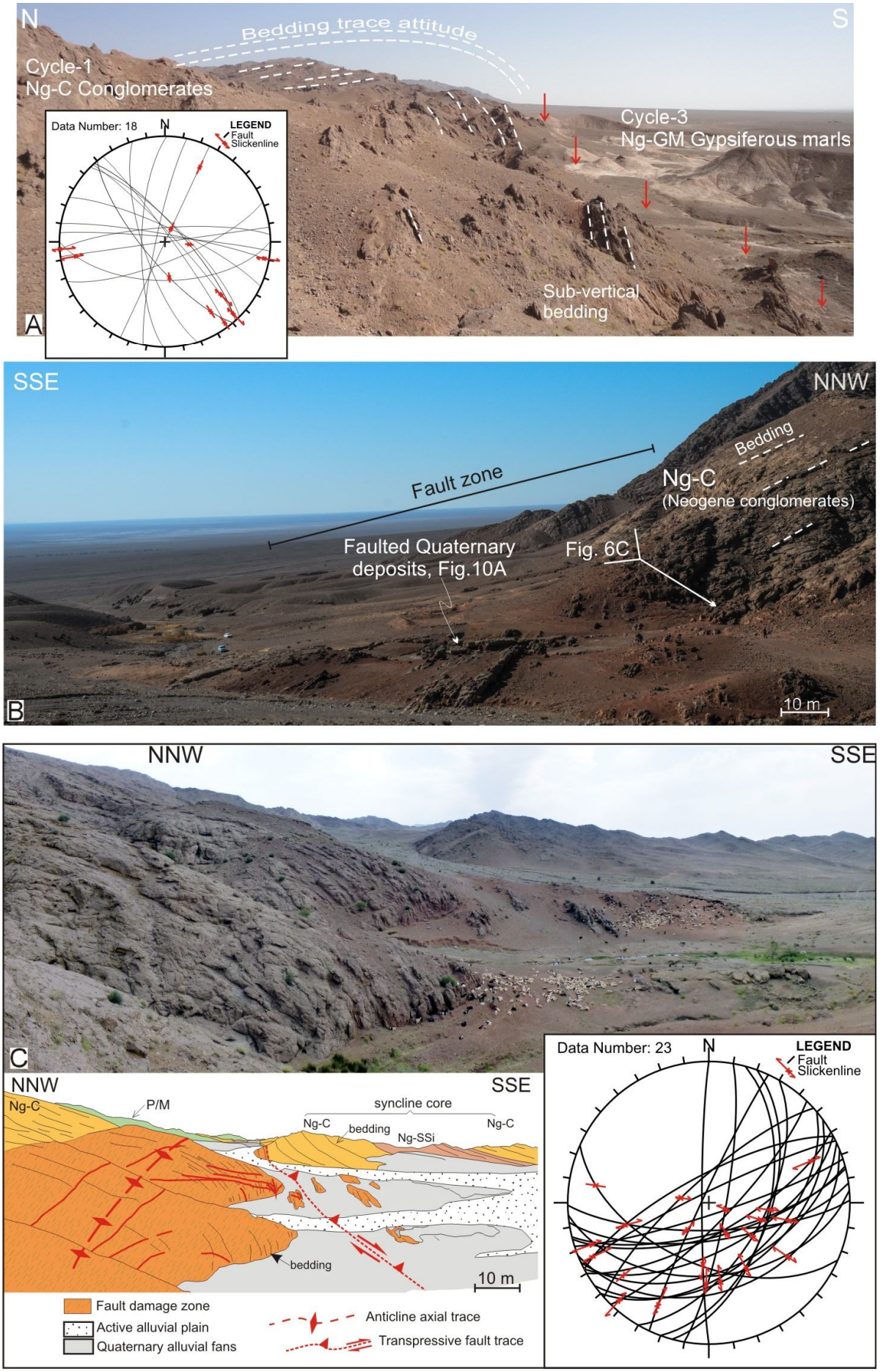
N
S
Bedding trace attitude
Cycle-1
Ng-C Conglomerates
Data Number: 18
N
LEGEND
Fault
Slickenline
Cycle-3
Ng-GM Gypsiferous marls
Sub-vertical
bedding
A
SSE
NNW
Bedding
Fault zone
Ng-C
(Neogene conglomerates)
Faulted Quaternary
deposits, Fig.10A
Fig. 6C
10 m
B
NNW
SSE
C
NNW
SSE
Ng-C
P/M
syncline core
Ng-C
bedding
Ng-SSi
Ng-C
bedding
10 m
Fault damage zone
Active alluvial plain
Quaternary alluvial fans
Anticline axial trace
Transpressive fault trace
Data Number: 23
N
LEGEND
Fault
Slickenline

1540

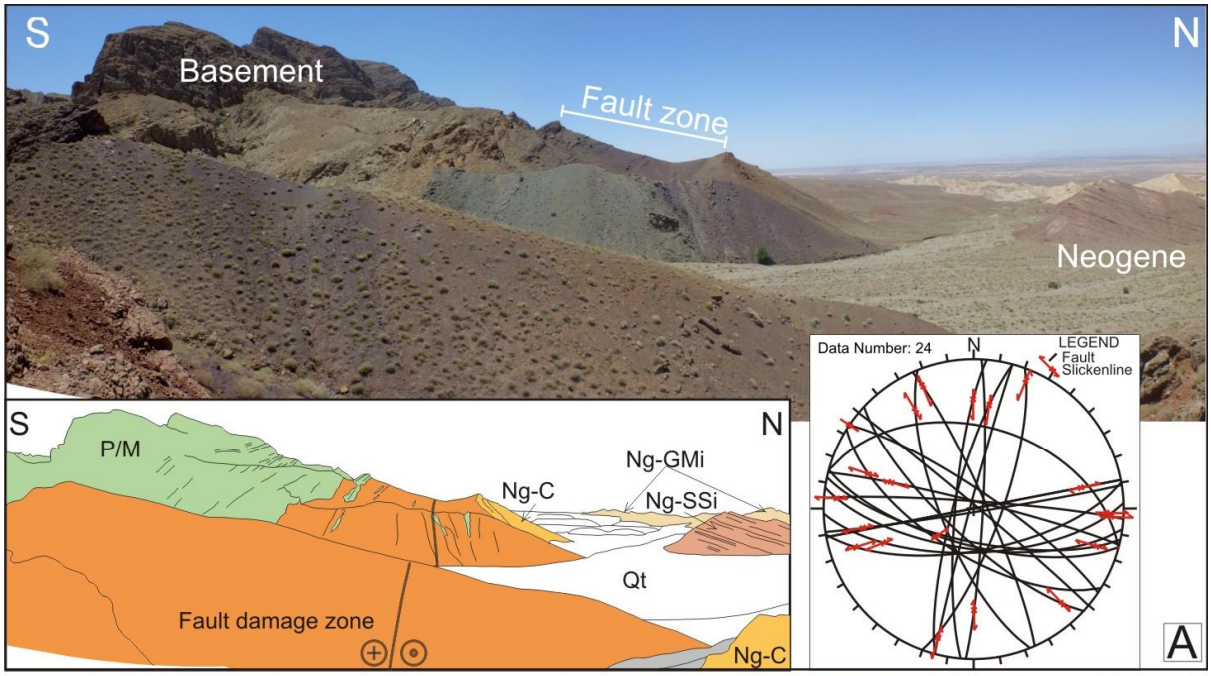
S
N
Basement
Fault zone
Neogene
S
N
P/M
Ng-GMi
Ng-C
Ng-SSi
Qt
Fault damage zone
Ng-C
Data Number: 24
N
LEGEND
Fault
Slickenline
A

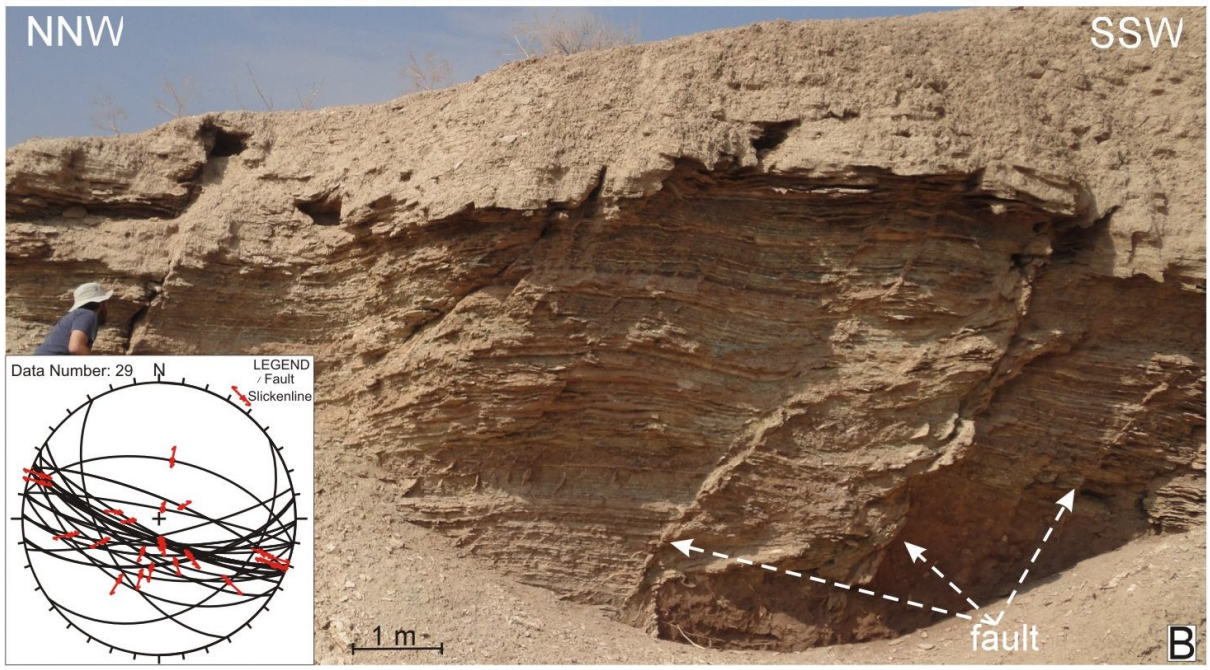
NNW
SSW
Data Number: 29
N
LEGEND
Fault
Slickenline
1 m
fault
B

1541

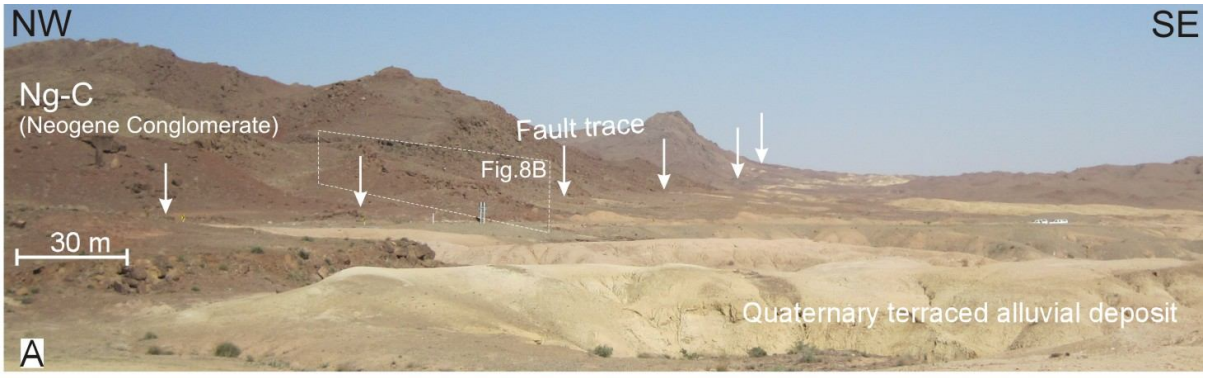
NW
SE
Ng-C
(Neogene Conglomerate)
Fault trace
Fig.8B
30 m
Quaternary terraced alluvial deposit
A

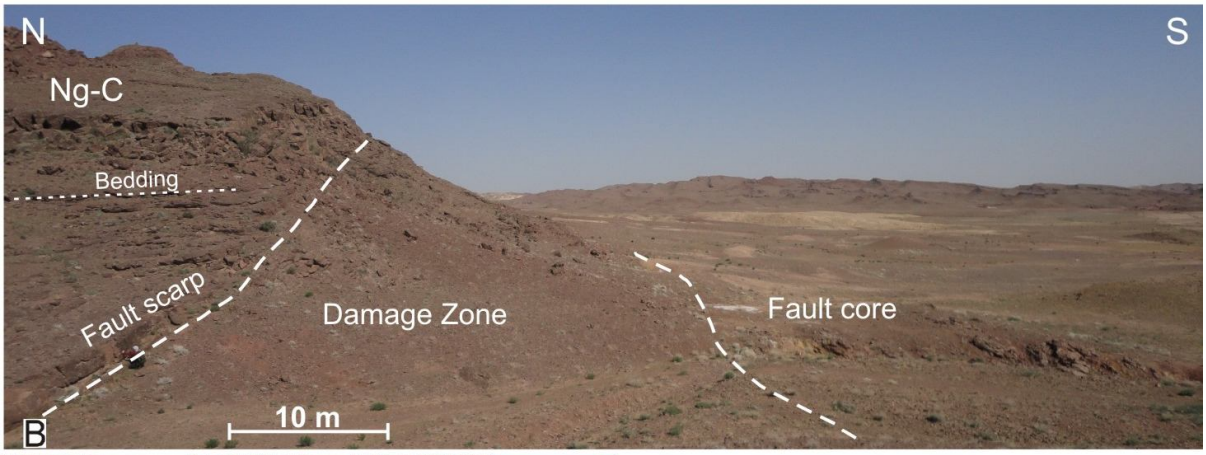
N
S
Ng-C
Bedding
Fault scarp
Damage Zone
Fault core
10 m
B

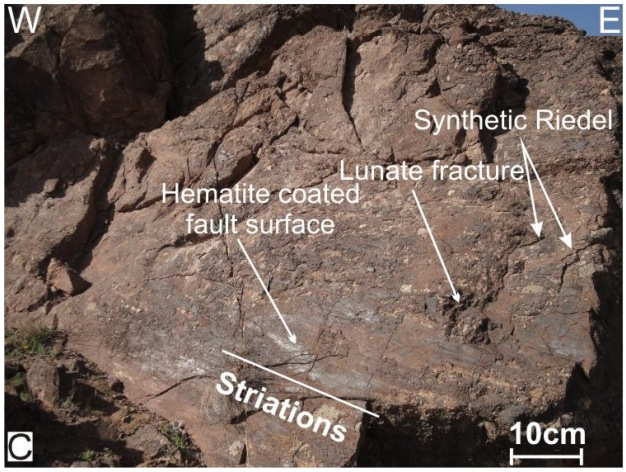
W
E
Synthetic Riedel
Lunate fracture
Hematite coated
fault surface
Striations
10cm
C

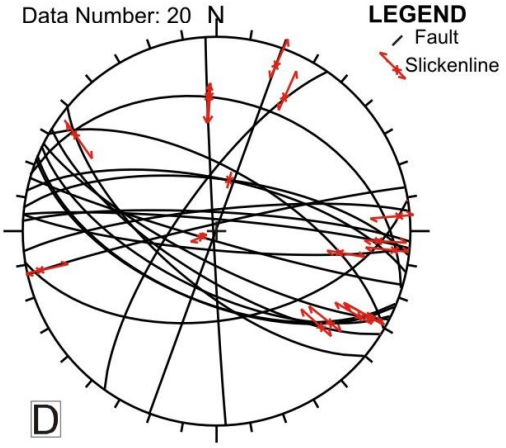
Data Number: 20
N
LEGEND
Fault
Slickenline
D

1542

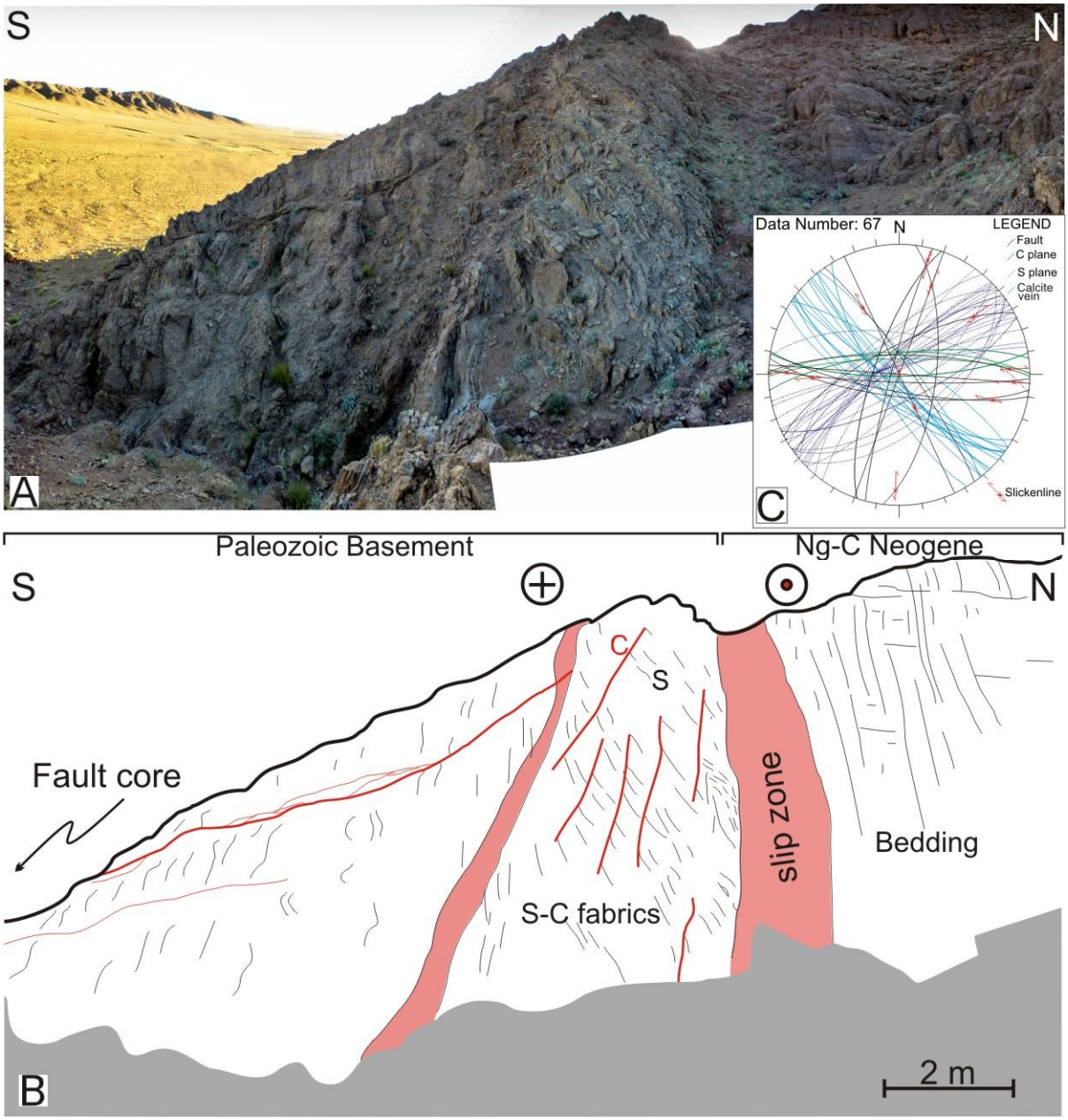
S
N
A
Data Number: 67
N
LEGEND
Fault
C plane
S plane
Calcite vein
Slickenline
C
Paleozoic Basement
Ng-C Neogene
S
N
C
S
Fault core
slip zone
Bedding
S-C fabrics
B
2 m

1543

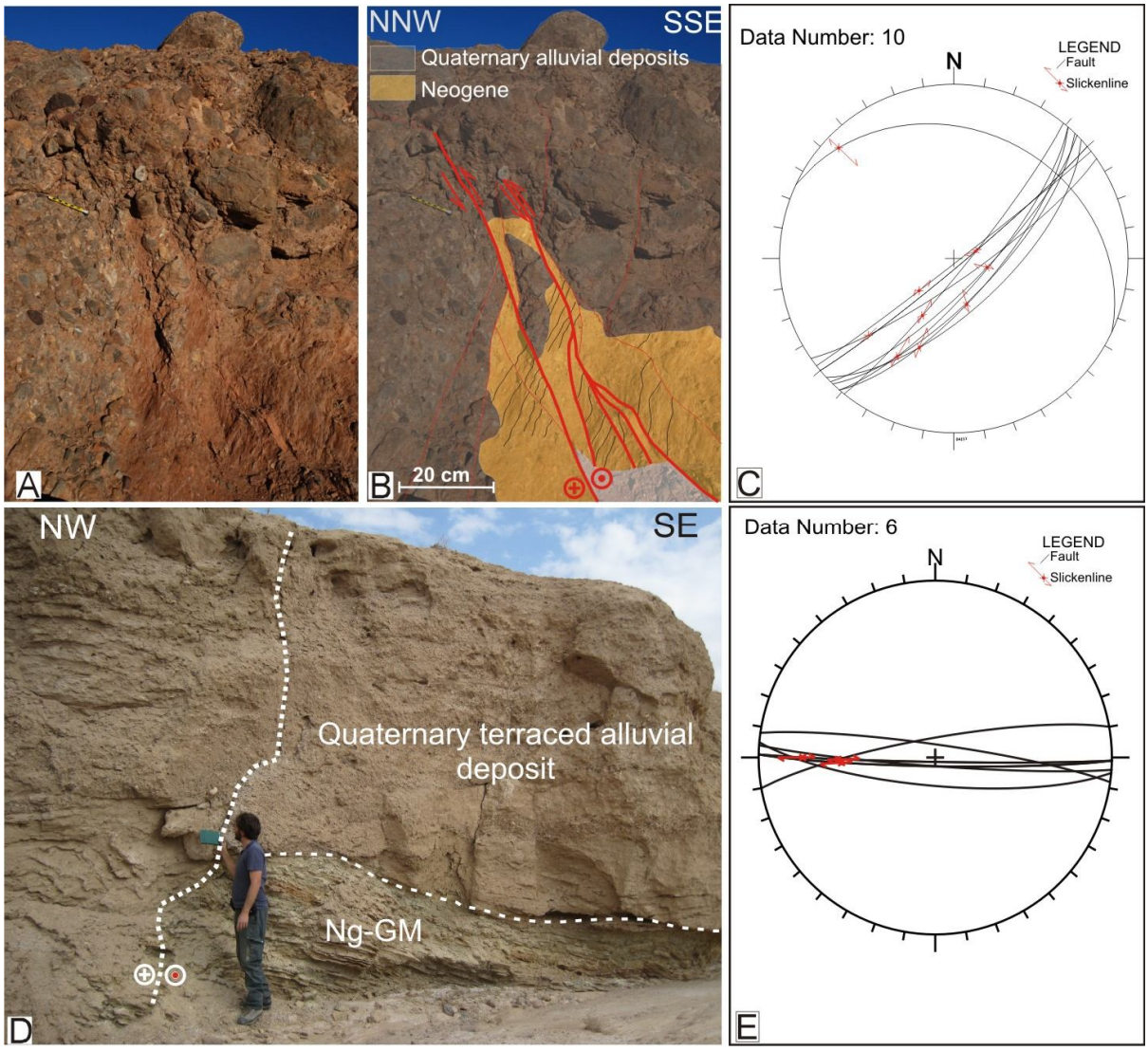
A
NNW
SSE
Quaternary alluvial deposits
Neogene
B
20 cm
Data Number: 10
N
LEGEND
Fault
Slickenline
C
NW
SE
Quaternary terraced alluvial deposit
Ng-GM
D
Data Number: 6
N
LEGEND
Fault
Slickenline
E

1544

1545

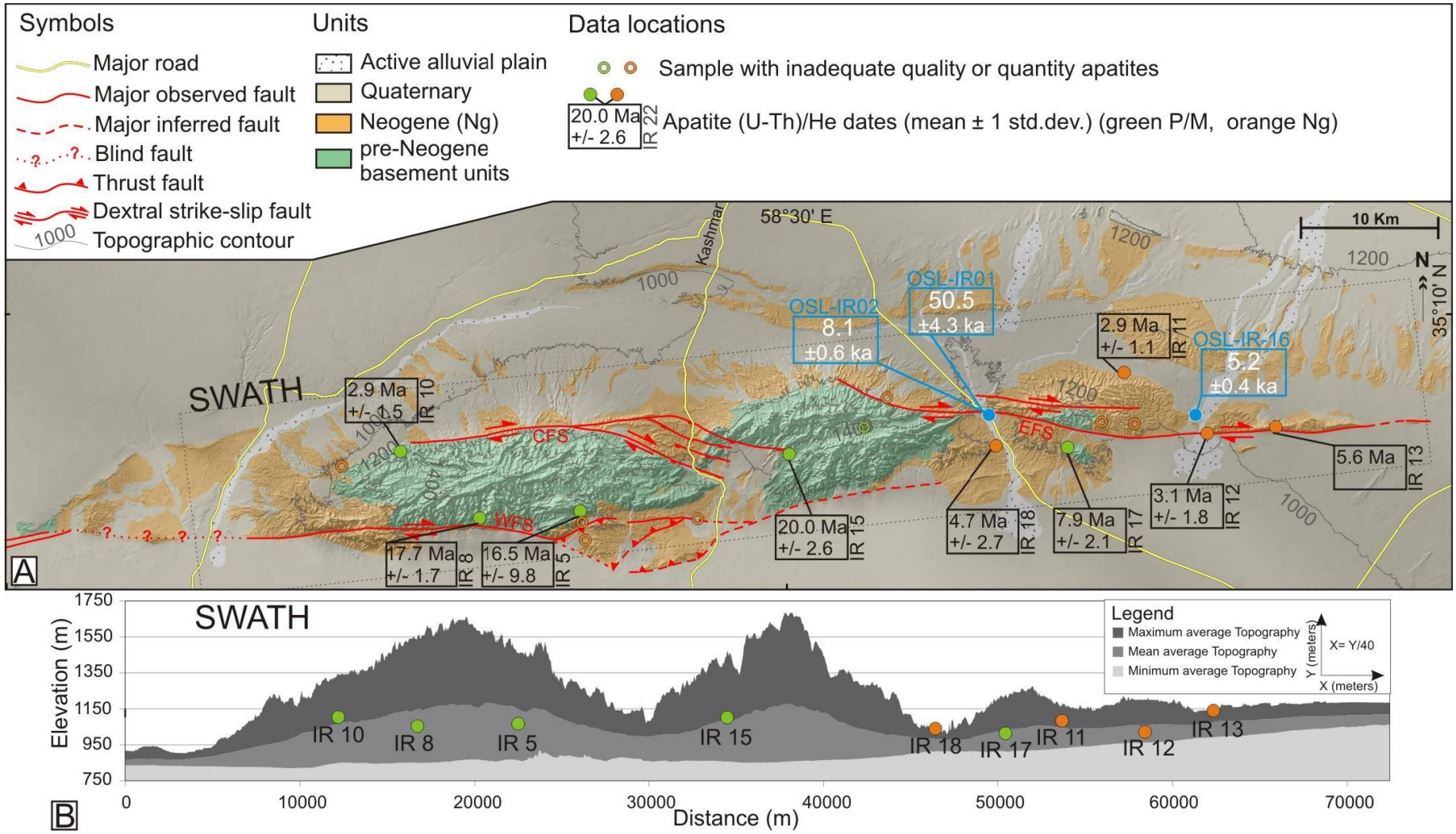
Symbols
Major road
Major observed fault
Major inferred fault
Blind fault
Thrust fault
Dextral strike-slip fault
1000
Topographic contour
Units
Active alluvial plain
Quaternary
Neogene (Ng)
pre-Neogene basement units
Data locations
Sample with inadequate quality or quantity apatites
20.0 Ma +/- 2.6 IR 22
Apatite (U-Th)/He dates (mean ± 1 std.dev.) (green P/M, orange Ng)
58°30' E
10 Km
N
35°10' N
Kashmar
SWATH
CFS
WFS
EFS
OSL-IR01 50.5 ±4.3 ka
OSL-IR02 8.1 ±0.6 ka
OSL-IR-16 5.2 ±0.4 ka
2.9 Ma +/- 1.5 IR 10
17.7 Ma +/- 1.7 IR 8
16.5 Ma +/- 9.8 IR 5
20.0 Ma +/- 2.6 IR 15
4.7 Ma +/- 2.7 IR 18
7.9 Ma +/- 2.1 IR 17
2.9 Ma +/- 1.1 IR 11
3.1 Ma +/- 1.8 IR 12
5.6 Ma IR 13
A
SWATH
Legend
Maximum average Topography
Mean average Topography
Minimum average Topography
X= Y/40
Y (meters)
X (meters)
Elevation (m)
Distance (m)
IR 10
IR 8
IR 5
IR 15
IR 18
IR 17
IR 11
IR 12
IR 13
B

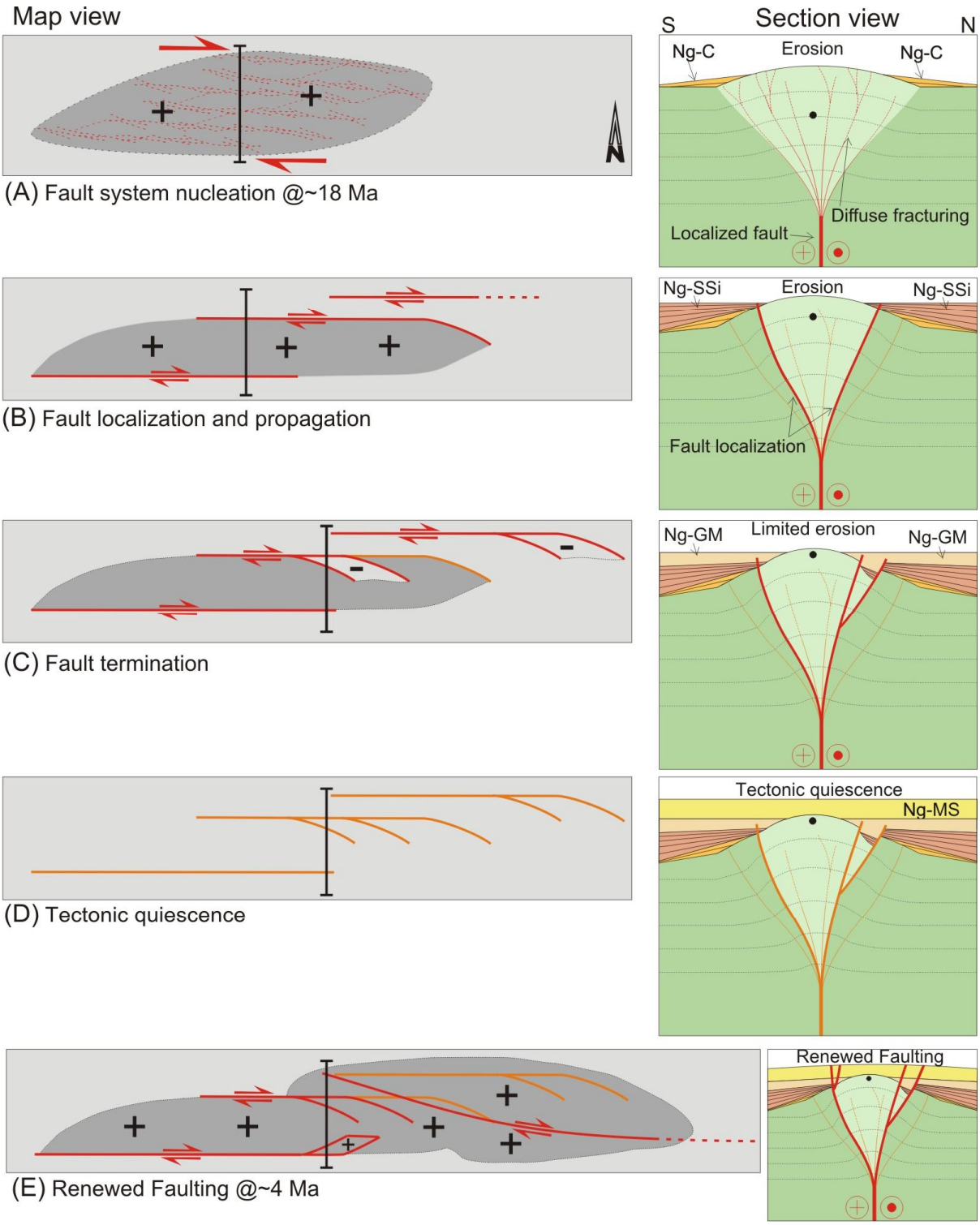
Map view
Section view
S
N
Ng-C
Erosion
Ng-C
Diffuse fracturing
Localized fault
(A) Fault system nucleation @~18 Ma
Ng-SSi
Erosion
Ng-SSi
Fault localization
(B) Fault localization and propagation
Ng-GM
Limited erosion
Ng-GM
(C) Fault termination
Tectonic quiescence
Ng-MS
(D) Tectonic quiescence
Renewed Faulting
(E) Renewed Faulting @~4 Ma

1547